Author manuscript of article published in *Biomaterials Science*, https://doi.org/10.1039/D2BM01149B

Aqueous synthesis and self-assembly of bioactive and thermo-responsive HA-*b*-ELP bioconjugates

Manon Levêque,[a] Ye Xiao,[a] Laura Durand,[a] Louise Massé,[a] Elisabeth Garanger,*[a] and Sébastien Lecommandoux*[a]

[a] Université de Bordeaux, CNRS, Bordeaux INP, LCPO, UMR 5629, Pessac F-33600, France.

Corresponding authors: garanger@enscbp.fr and lecommandoux@enscbp.fr

KEYWORDS

Elastin-like polypeptides (ELPs), hyaluronan (HA), strain-promoted azide-alkyne cycloaddition (SPAAC), thermo-responsive bioconjugates, self-assembled nanoparticles, phase diagram, CD44 targeting

GRAPHICAL ABSTRACT

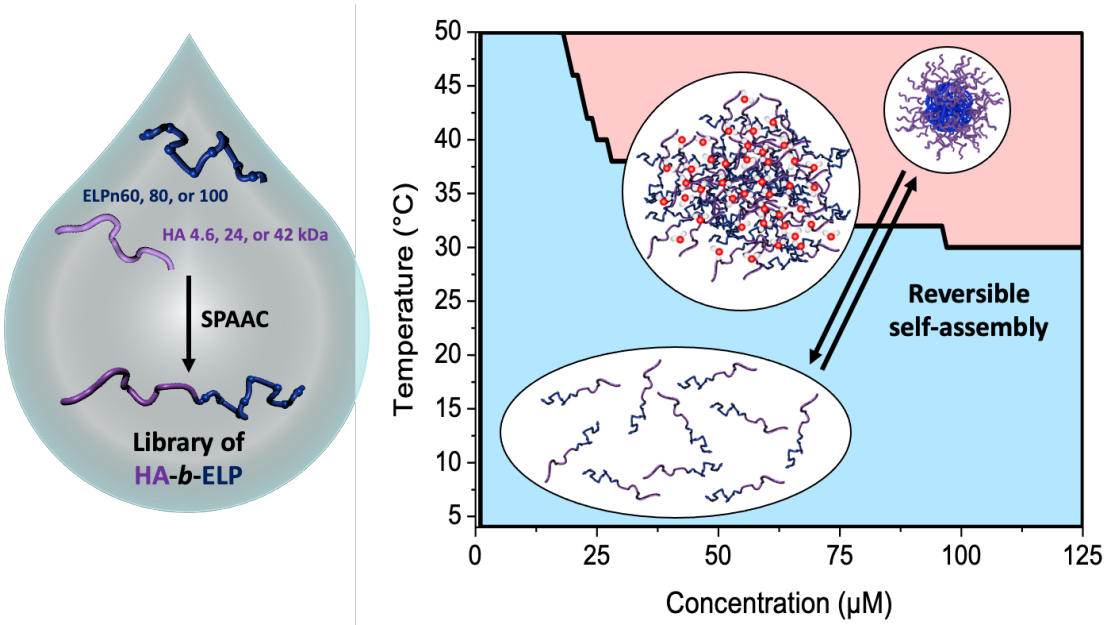

ABSTRACT

The design of synthetic (bio)macromolecules that combine biocompatibility, self-assembly and bioactivity properties at the molecular level is an intense field of research for biomedical applications such as (nano)medicine. In this contribution, we have designed and synthesized a library of bioactive and thermo-responsive bioconjugates from elastin-like polypeptides (ELPs) and hyaluronic acid (HA) in order to access bioactive self-assembled nanoparticles These were prepared by a simple synthetic and purification strategy, compatible with the requirements for biological applications and industrial scale-up. A series of 9 HA-*b*-ELP bioconjugates with different compositions and block lengths was synthesized in aqueous conditions by strain-promoted azide-alkyne cycloaddition (SPAAC) avoiding the use of catalyst, co-reactant and organic solvent, and isolated by a simple centrifugation step. An extensive physico-chemical study was then achieved on the whole library of bioconjugates to attempt to establish structure-properties relationships. In particular, the determination of the critical conditions for thermally-driven self-assembly was carried out upon temperature (CMT) and concentration (CMC) gradients, leading to a phase diagram for each of these bioconjugates. These parameters as well as the size of nanoparticles were found to depend on the chemical composition of the bioconjugates, namely on the respective size of individual blocks. Understanding the mechanism underlying this dependency is a real asset for designing more effective experiments: with key criteria defined (*e.g.* concentration, temperature, salinity, biological target), the composition of the best candidates can be rationalized. In particular four of the bioconjugates ($HA_{4.6k}$-ELPn80 or n100 and HA_{24k}-ELPn80 or n100) were found to self-assemble into well-defined spherical core-shell nanoparticles, with a negative surface charge due to the HA block exposed at the surface, a hydrodynamic diameter comprised between 40-200 nm in physiological conditions and a good stability over time at 37°C. We therefore propose here a versatile and simple design of smart, controllable, and bioactive nanoparticles that present different behaviors depending on diblocks' composition.

INTRODUCTION

For many years, significant efforts have been dedicated to the design of synthetic (bio)macromolecules that combine biocompatibility, self-assembly and bioactivity properties at the molecular level for specific applications, in particular for the field of (nano)medicine. Among these, elastin-like polypeptides (ELPs) have arose as promising biocompatible and stimuli-responsive protein-like polymer scaffolds.[1,2] Inspired from a natural structural protein (*i.e.*, elastin), ELPs are artificial recombinant polypeptides,[3] behaving simultaneously as intrinsically disordered proteins (IDPs) and random-coil polymers in θ-solvent in their soluble form in aqueous media.[4,5] Most common ELPs are based on consecutive repeats of "Val-Pro-Gly-Xaa-Gly" pentapeptides, Xaa being a guest residue that can be any natural or non-natural residue except for proline.[6] Efficiently produced in *Escherichia coli* (*E. coli*) bacteria and purified by a chromatography-free technique termed Inverse Transition Cycling (ITC),[7,8] recombinantly produced ELPs are polypeptides characterized by an exquisite control in primary sequence (including monomer sequence and chain length) unachievable with current polymerization techniques. Perfect batch-to-batch reproducibility from bacterial clones and exact molar masses allow the establishment of precise structure-properties relationships. A major characteristic of ELPs is their lower critical solubility temperature (LCST) transition behavior in aqueous media.[9,10] At a specific concentration, an ELP of a defined sequence and chain length is soluble below a cloud point temperature (T_{cp}) and insoluble above the latter. This cloud point temperature depends on several macromolecular and environmental parameters, such as the primary sequence of the ELP (guest residue composition), overall hydrophili/-phobicity of the polypeptide chain,[10–13] the presence and concentration of salts,[14,15] ionic strength, and ELP molar concentration following a logarithmic law.[12] Importantly, the LCST is the lowest T_{cp} among all concentrations considered and is defined as a critical point (C_c; $T_{cp,c}$) characteristic of a family of ELPs with a defined monomer sequence but of any chain length.[11] At any concentration, the aggregation of an ELP above the T_{cp} is perfectly reversible, with a re-solubilization into free chains upon cooling the aqueous solution below the T_{cp}. This property represents a real advantage in the design of "smart" polymer materials, and in particular for the formulation of self-assembled nanoparticles. In multiblock copolymer systems, the presence of an ELP block can induce a thermo-dependent amphiphilicity, leading to self-assembly into different (nano)objects.[16] The resulting self-assemblies strongly depend on the nature of the other block(s). For instance, in the case of a hybrid diblock copolymer, where the ELP is combined to a hydrophilic polymer segment (*e.g.,* polysaccharide,[17] PEG,[18] PLA[19]), the resulting bioconjugate is soluble below the T_{cp} of the ELP and self-assembled into micelle-like nanoparticles above the latter (the T_{cp} is therefore termed critical micellar temperature, CMT). On the contrary, the coupling of an ELP to more hydrophobic species (*e.g.,* drugs,[20,21] lipids,[22–24] polymers[25]) leads to an assembled system at low temperature that macroscopically aggregates upon heating of the solution and dehydration-induced aggregation of the ELP. In the case of an ELP diblock copolymer, in

which the T_{cp} of the two ELPs are significantly different, three physical states can be observed with increasing temperature: free chains in cold aqueous medium (*i.e.*, below the T_{cp} of the most hydrophilic block), micelles above the CMT and below the T_{cp} of the most hydrophobic block, and macroscopic aggregates above the latter (termed bulk T_{cp}).[5,26–29] At last, a copolymer composed of an ELP block and a UCST-polymer block (*e.g.,* resilin-like polypeptide) will present an inversion of micelle behavior: at low temperature, the UCST-block is hydrophobic while the ELP is hydrophilic, therefore assembled into micelles with a UCST-polymer core and an ELP corona.[30] The situation is reversed at higher temperature, with a hydrophobic ELP core and a hydrophilic UCST-polymer corona. In between, the system can be either all soluble or all aggregated depending on the relative values of the cloud point and clearing point temperatures (T_{cp} and T_{cl}) of the two blocks. This behavior is of significant interest as it enables the selective exposure of different ligands by coupling them to one or the other block. ELPs are therefore particularly relevant precision polymers for biomedical applications, in particular for nanomedicine: they are bioinspired, biocompatible, stimuli-responsive, and their integration in multiblock polymer systems allows a precise control of their self-assembly properties.[1,31–34] However, because they lack intrinsic bioactivity, several strategies have been explored for their use as effective drug-delivery nanocarriers.[1,34] In particular, targeting moieties have been added either by genetic engineering or by chemical post-modifications of recombinant ELPs.[35–44]

In the present work, we have particularly explored the possibility to conjugate ELPs to hyaluronan (HA) as CD44 targeting ligand.[45,46] CD44 is a receptor that is overexpressed at the surface of tumor cells in many cancers.[47–52] Notably, it is considered as a reliable marker for cancerous stem cells (CSCs) that are suspected to be responsible for relapses after treatment.[53–58] Its main ligand is HA,[59] a polysaccharide naturally present in the organism, mostly in the skin and cartilage, hence its high biocompatibility and biodegradability.[45] Its chemical and physicochemical properties make it an excellent candidate for the design of drug delivery systems,[60,61] among other biological applications. In particular, its high hydrophilicity provides it with great hydration capacities that have made it an inescapable ingredient in the cosmetic field.[62,63] It is thus already approved by the FDA for cosmetic and pharmaceutic use and produced at industrial scale.[64] Interestingly, ELPs and HA have already been combined either in mixed formulations or as covalent conjugates, but mainly for tissue engineering and cell culture applications. Their association for the design of smart nanocarriers is to our knowledge still unexplored.

In a previous study, we have described the synthesis of a small library of oligo- or polysaccharide-*b*-ELP bioconjugates, including a HA-*b*-ELP bioconjugate based on a 7 kDa HA and 17 kDa ELP.[17] These bioconjugates were synthesized by copper-catalyzed azide-alkyne cycloaddition (CuAAC) in organic solvent. Once isolated, these were shown to spontaneously self-assemble in water into nanometer-sized particles upon heating and to reversibly disassemble upon cooling back the solution. In particular, the CMT of the HA-*b*-ELP bioconjugate ranged between 37°C at 800 µM and 58°C at 30

μM, and formed sub-micron sized particles (ca 200-300 nm) above the CMT, values that were poorly relevant with our target application (*i.e.*, nanomedicine). In this contribution, we therefore aimed at providing a straightforward synthetic design to afford well-defined HA-*b*-ELP bioconjugates and explore their self-assembly. The synthetic strategy was first developed to be carried out in water and without the use of catalyst and co-reactants. ELPs with various chain lengths were explored to lower the CMT in a physiologically-relevant temperature domain and to minimize its dependance with molar concentration of the bioconjugates. Different sizes of HA were also considered to study the effect of the size of the hydrophilic block on nanoparticles' properties. A total of 9 HA-*b*-ELP bioconjugates were therefore synthesized, characterized and their self-assembly in aqueous media was extensively explored. In particular, the determination of CMCs at different temperatures and CMTs at different concentrations allowed the establishment of phase diagrams for all bioconjugates, allowing the prediction of their soluble or self-assembled state in subsequent biological studies.

RESULTS AND DISCUSSION

The diblock HA-*b*-ELP bioconjugate previously reported by our group comprised a 7 kDa HA segment covalently linked to a 40 repeat unit-ELP (ELP[M_1V_3-40]) of 17,035 $g.mol^{-1}$.[17] For the present work, the primary sequence of the ELP was conserved, *i.e.*, $[(VPGVG)(VPGMG)(VPGVG)_2]_m$, noted as ELP[$M_1V_3$-n] with n the total number of (VPGXG) pentapeptide repeats (n=4*m). However, this HA_{7k}-*b*-ELP[M_1V_3-40] displays a high CMT and a strong dependency of the CMT over molar concentration, which is typical of short ELPs, and can compromise the stability of self-assembled nanoparticles over a large concentration range. We have thus decided to increase the length (and therefore molar mass) of the ELPs used for this study, and explored three different ELP[M_1V_3-n] with n = 60, 80, and 100 (shortened as ELPn60, ELPn80 and ELPn100 in this manuscript). These ELPs were produced recombinantly in *E. coli* bacteria following previously reported procedures.[65] Their detailed characterization is provided in **Figures S1-S5**. Three sizes of HA were also selected, namely HA of 4.6, 24 and 42 kDa. The synthesis of the 9 HA-*b*-ELP bioconjugates (thereafter noted HA_{xk}-ELPnZ, x corresponding to the molar mass of the HA segment and Z to the number of pentapeptide repeats) was achieved in water by strain promoted azide-alkyne cycloaddition (SPAAC) in order to avoid the use of copper catalyst, co-reactant and organic solvent as compared to our previous synthetic strategy.[17] To this end, the different HA segments were modified at the reducing chain end to introduce an azido group, while the three ELPs were modified at the *N*-terminal chain end to provide them with a dibenzocyclooctyne (DBCO) moiety, the strain induced by the cyclic structure making the alkyne highly reactive and enabling a catalyst-free cycloaddition reaction.[66–68] (**Figure 1**)

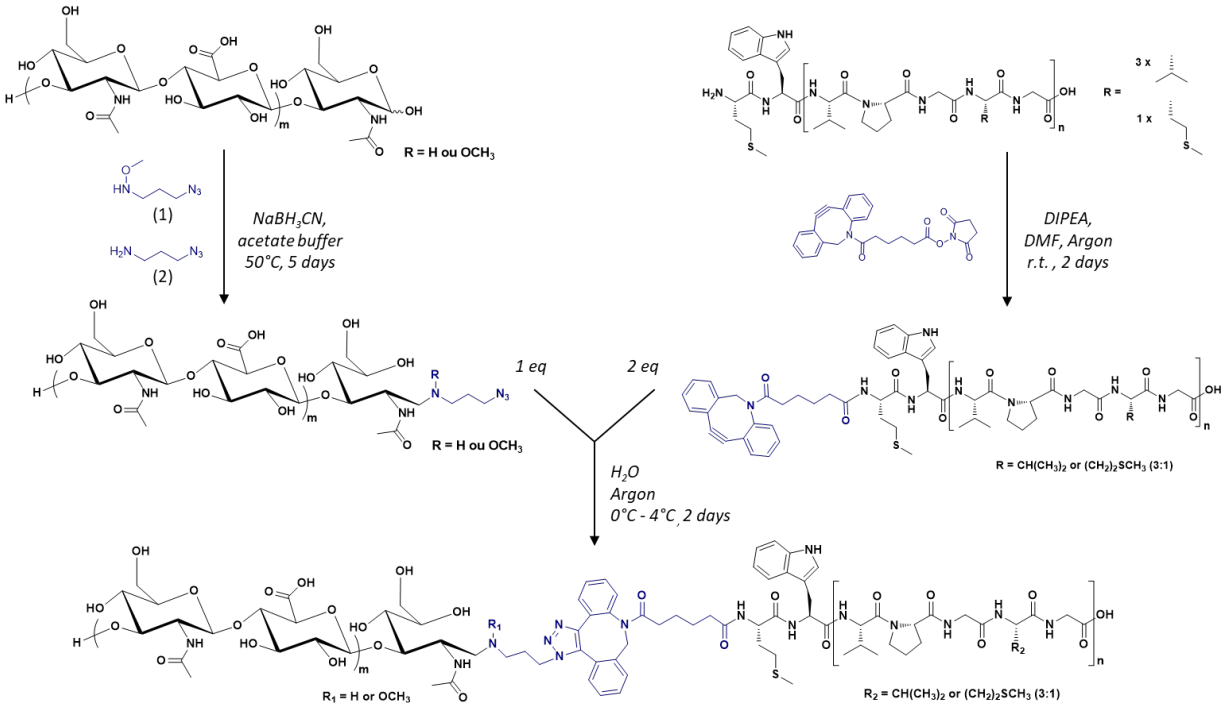

Figure 1: *General synthetic scheme of the library of HA-b-ELP bioconjugates by SPAAC, using azido-functionalized HA segments (left) and DBCO-functionalized ELPs (right).*

In a first step, the anomeric position of the three HA segments was functionalized with an azido group through reductive amination in presence of $NaBH_3CN$ at 50°C. (**Figure 1**) *N*-(3-azidopropyl)-*O*-methylhydroxylamine (1), a home-made reagent favoring the closed form of the last sugar unit,[17,69] was used for HA 4.6 kDa, while the commercially available azidopropanamine (2) was used for HA 24 and 42 kDa. The ELP block was functionalized at the *N*-terminal chain end by amidation reaction using a commercially available heterobifunctional cross-linking agent containing a DBCO moiety and a *N*-hydroxysuccinmide-activated ester group. The choice of DBCO as constrained alkyne was motivated by its stability, reactivity, and commercial availability. The three HA-N_3 (*i.e.*, 4.6, 24 and 42 kDa) and the three DBCO-ELP (n60, n80 and n100) were obtained in good yields and fully characterized by ^{1}H NMR, MALDI and SEC. (**Figures S6-S7**) For the 9 HA-*b*-ELP bioconjugates, the consecutive SPAAC reactions were carried out in pure water, using a 2-fold excess of DBCO-ELP. In order to avoid ELP oxidation (at methionine residues) and aggregation, the reactions were performed at 4°C under inert atmosphere. After 2 days, HA-*b*-ELP bioconjugates were isolated and excess DBCO-ELP removed by a simple centrifugation at 40°C, the diblock HA-*b*-ELP remaining in the supernatant while the excess ELP aggregated was eliminated in the pellet. The success of the reactions and purifications was confirmed by gel electrophoresis (SDS-PAGE) as illustrated on **Figure 2A** for the $HA_{4.6k}$-ELPn80 bioconjugate.

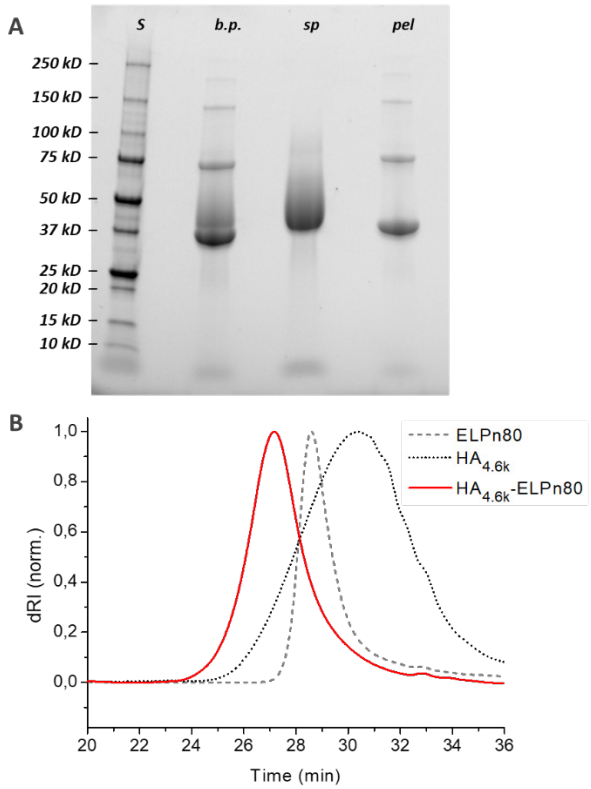

Figure 2: *Characterization of the $HA_{4.6k}$-ELPn80 bioconjugate by SDS-PAGE (A) and SEC (B). A: S: protein size markers; b.p.: reaction medium before purification; sp: supernatant; pel: pellet. B: samples in phosphate buffer.*

Before purification, the line on the protein gel (**Figure 2A**, line *b.p.*) shows both neat black bands, characteristic of well-defined proteins, and a smear corresponding to polydisperse macromolecules. Indeed, while ELPn80 has a narrow dispersity due to its recombinant production (leading to neat bands on the gel), the $HA_{4.6k}$ obtained by degradation of longer HA chains presents a high dispersity (as noticeable on the size exclusion chromatogram, **Figure 2B**). The combination of the two blocks therefore leads to a polydisperse $HA_{4.6k}$-ELPn80 bioconjugate appearing as a smear. After purification, this smear is observed only in the supernatant (**Figure 2A**, line *sp*), whereas the precise bands corresponding to the excess ELPn80 used in the reaction (and to its non-covalent multimers) were recovered in the pellet (**Figure 2A**, line *pel*). This confirmed the efficient separation of the $HA_{4.6k}$-ELPn80 bioconjugate from DBCO-ELPn80 used in excess. Bioconjugates were also analysed by size exclusion chromatography (SEC). The chromatogram in **Figure 2B** shows the elution times of the two individual blocks ELPn80 and $HA_{4.6k}$ in gray, confirming their difference in molar mass and molecular dispersity. In red, the curve of the final product, $HA_{4.6k}$-ELPn80, appears shifted towards shorter elution times, in agreement with the increased hydrodynamic diameter of the bioconjugate and greater molar mass. Characterizations by SDS-PAGE and SEC for the entire library of bioconjugates are provided in **Figures S8** and **S9**, respectively. Altogether these analyses confirmed the efficiency of

both the SPAAC reaction and the simple purification method for the $HA_{4.6k}$-ELPn80 bioconjugate. All bioconjugates, combining the three HA of different molar masses (4.6, 24, 42 kDa) and the three ELPs of different molar masses (25.4, 33.7, 42 kDa) were synthetized, purified and characterized following a similar procedure. A summary of the molecular characteristics and composition of the 9 HA-*b*-ELP bioconjugates of the library is provided in **Figure 3**.

A

$Mw_{bioconjugate}$ (kDa) ($\%\ Mw_{HA}$ / Mw_{total})		HA		
ELP [M_1V_3-n]		4.6 kDa	24 kDa	42 kDa
n = 60	25.4 kDa	30.4 (15 $\%_{HA}$)	49.8 (48 $\%_{HA}$)	67.8 (62 $\%_{HA}$)
n = 80	33.7 kDa	38.7 (12 $\%_{HA}$)	58.1 (41 $\%_{HA}$)	76.1 (55 $\%_{HA}$)
n = 100	42 kDa	47.0 (10 $\%_{HA}$)	66.4 (36 $\%_{HA}$)	84.4 (50 $\%_{HA}$)

B

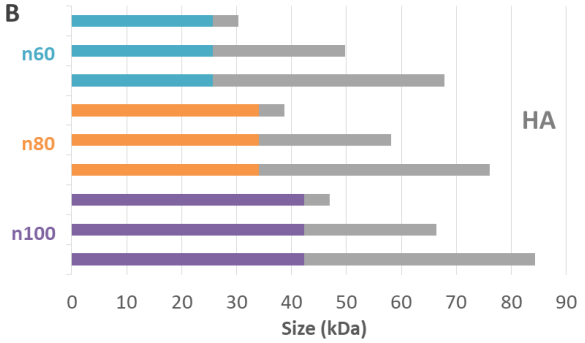

Figure 3: *Description of the library of the HA-b-ELP bioconjugates. (A) Table of molar masses and mass fractions of HA in the bioconjugates. The additional 0.4 kDa in the bioconjugate as compared to the addition of molar mass of individual block corresponds to the molar mass of the cross-linker. (B) Schematic representation of the composition of bioconjugates.*

Most of the synthesized bioconjugates present a hydrophilic block (HA) shorter than the thermosensitive one (ELP). Two of them have rather equivalent composition (namely HA_{24k}-ELPn60 and HA_{42k}-ELPn100), and two others have a larger HA segment as compared to the ELP (namely HA_{42k}-ELPn60 and HA_{42k}-ELPn80). This library of HA-*b*-ELP bioconjugates presenting different molar masses and compositions allowed us to perform an extensive physicochemical characterization to understand their thermal behavior in aqueous conditions. We anticipated the difference in hydrophilicity to have a strong impact on the thermo-responsive behavior of the bioconjugates, influencing their self-assembly properties. From a biological perspective, the variation of HA molar masses implies a difference in the strength of its interaction with the CD44 receptor,[70] which has a significant impact for the targeted nanomedicine applications.

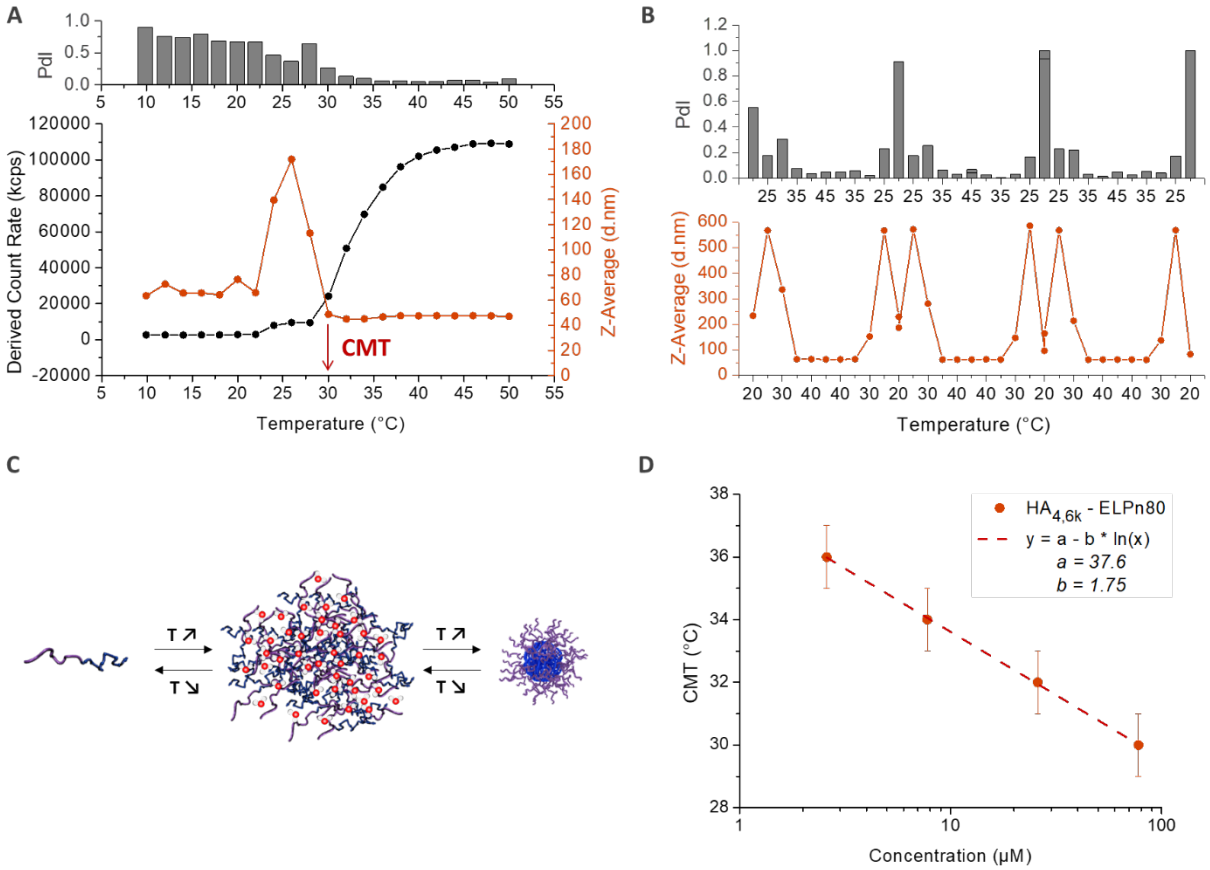

Figure 4: *Characterization of the self-assembly behavior of $HA_{4,6k}$-ELPn80 conjugate in PBS. A: Determination of the Critical Micellar Temperature (CMT) by DLS analysis of a solution at 78 µM in PBS upon a heating ramp (10°C-50°C). B: Monitoring of the reversibility of the self-assembly during 3 cycles of temperature ramps (20°C-45°C) for a solution at 80 µM in PBS. C: Representation of the reversible bioconjugates' self-assembly with temperature. D: Evolution of the CMT with concentration. Fit: CMT = a – b * ln(C).*

The thermo-responsive properties of all bioconjugates were then studied by dynamic light scattering (DLS). A typical example for the bioconjugate $HA_{4.6k}$-ELPn80 at 80 µM (typical concentration used for subsequent biological studies to be reported elsewhere) in PBS is given in **Figure 4**. As illustrated in **Figure 4A**, the scattered intensity, also referred to as the derived count rate (DCR), is very low below 24°C, which is characteristic of small diffusive objects. The z-average varies around 60 nm, but the high polydispersity index (PdI) indicates the presence of few poorly defined aggregates. Under this temperature, the system is therefore mainly composed of free chains in solution with the presence of some aggregates. Between 24°C and 30°C, a little increase in the DCR can be observed, coupled with a small decrease of the PdI. But the major change is the evolution of the z-average, which increases sharply to reach 180 nm and decreases also abruptly to reach 40 nm. This phase is the hallmark of a coacervation process, with large objects highly hydrated, hence poorly scattering. Finally, from 30°C, a 3rd phase is observed. The z-average stabilizes around 40 nm, with a very low PdI (<0.1), indicating the presence of only one population of objects. The DCR increases and is followed by a stabilization around 110,000 kcps, which relates to the densification of nanoparticles' core by dehydration of the

ELP, in agreement with previously reported examples on self-assembly of ELP diblock copolymers.[5] At 30°C and beyond, the solution therefore contains monodispersed nanoparticles with a hydrodynamic diameter (D_H) of 40 nm. The reversibility of the self-assembly process is illustrated in **Figure 4B**, with an inversed behaviour upon cooling. A schematic representation of the observed self-assembly behavior is illustrated in **Figure 4C**. The previous conclusions are also supported by the representation of the size distribution (expressed in intensity) and correlograms obtained for this solution at 5°C and 50°C (**Figure S10)**: while several populations and small objects are observed at low temperature, there is only one population of 40 nm-sized nanoparticles upon heating above the CMT. The temperature characteristic of the self-assembly (CMT) is here defined as the temperature at which only nanoparticles are present in solution. It is thus determined as the first temperature value at which both the z-average and the PdI stabilize. As shown on **Figure 4A**, the CMT is therefore estimated at 30°C (± 1) for the $HA_{4.6k}$-ELPn80 bioconjugate. This CMT was determined at different concentrations and plotted in **Figure 4D**. Interestingly, a similar trend was observed for HA-*b*-ELP bioconjugates than for pure ELPs and in concordance with our previous observations on the HA_{7k}-ELPn40:[17] the CMT increases with dilution, following a logarithmic trend previously described by Chilkoti's group.[12] A similar self-assembly behaviour was observed for all of the 9 HA-*b*-ELP bioconjugates. (**Figure S11**) For all bioconjugates, the evolution of CMT with molar concentration also followed a similar logarithmic law. (**Figure S12)**

The CMT was also determined by fluorescence spectroscopy using Nile Red. Indeed, the fluorescence properties of Nile Red change as a function of the polarity of the medium.[71] In aqueous medium, Nile Red forms poorly soluble aggregates via Π-Π interactions that induce the quenching of the fluorescence.[72,73] In more hydrophobic medium, Nile Red interacts mainly with the solvent, dissolving the aggregates and recovering its fluorescence.[74,75] Nile Red is therefore often used to characterize the conditions of appearance of hydrophobic microdomains in solution, characteristic of micellization behavior.[72,75,76] Here, the self-assembly in nanoparticles above the CMT induces the formation of such hydrophobic microdomains in their core, leading to an increase of the fluorescence intensity of Nile Red. The simultaneous determination of the critical micellar temperature (CMT) and critical micellar concentration (CMC) is detailed in **Figure 5** for the $HA_{4.6k}$-ELPn80 bioconjugate. Fluorescence spectra were acquired every 2°C upon a heating ramp from 4°C to 50°C for solutions at 8 different concentrations. (**Figure 5A** illustrates fluorescence spectra obtained from 4°C to 50°C for a 100 µM concentration). The intensity of fluorescence at 637 nm was then plotted as function of temperature (**Figure 5B**) or concentration (**Figure 5C**). The CMT and CMC were respectively defined as the inflexion point of the curves or as the intersection of two logarithmic fits. This method was applied at each temperature and each concentration allowing to access to complete phase diagrams.

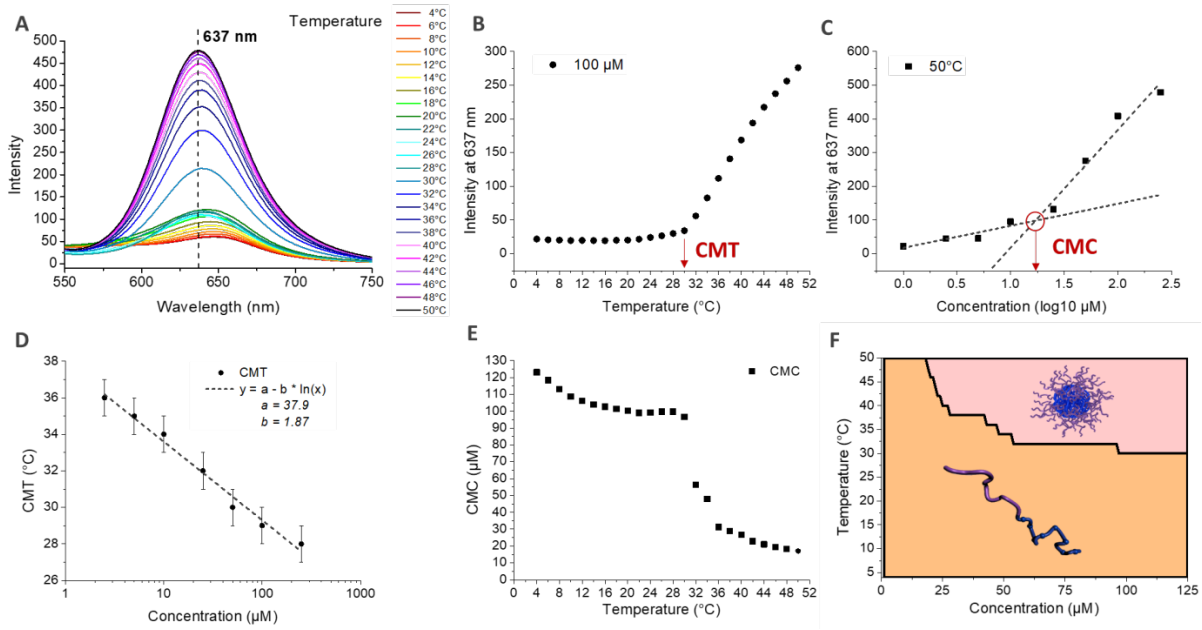

Figure 5: *Determination of the critical micellar temperature (CMT) and concentration (CMC) by fluorescence spectroscopy (polarity probe: Nile Red) for $HA_{4,6k}$-ELPn80 in PBS. (A) Stacking of the fluorescence emission spectra during a heating ramp (4°C-50°C) for a solution at 100 µM. λ_{ref} = 637 nm → wavelength at the maximal fluorescence intensity. (B) Evolution of the fluorescence intensity at λ_{ref} with the temperature at 100 µM. CMT = temperature at the inflexion point. (C) Evolution of the fluorescence intensity at λ_{ref} with the concentration at 50°C. Fit with two logarithmic models. CMC = concentration at the intersection. D: Evolution of the CMT with concentration. Fit: CMT = a – b * ln(C). (E) Evolution of the CMC with temperature. (F) Representation of the corresponding phase diagram (coacervate phase non-represented).*

In **Figure 5D**, the CMT is plotted as function of concentration. If the values here are similar to those determined by DLS, those for the other bioconjugates are somewhat lower. These observations are consistent, considering that for DLS, the CMT corresponds to the temperature at which there are only nanoparticles in solution (end of the transition), while by fluorescence, the CMT detected is the temperature at which the first hydrophobic clusters are detected (beginning of the transition). Nevertheless, similar logarithmic dependence of CMT with concentration is observed (**Figure 4D** and **Figure S13**). **Figure 5E** shows the evolution of the CMC with temperature. At low temperature, the CMC is high (above 100 µM) and slowly decreases with increasing temperature. At about 28°C, an abrupt decrease of the CMC is observed, up to about 36°C, consistently with the range of the corresponding CMT for this system. Above 36°C, the CMC retrieves its slow decrease, with values in the range 10-20 µM. The combination of these data allowed the elaboration of a phase diagram as function of both molar concentration and temperature, circumscribing the domains of $HA_{4.6k}$-ELPn80 present as free chains or as self-assembled nanoparticles. (**Figure 5F**). All of the 9 HA-*b*-ELP bioconjugates were studied and analysed in a similar manner, (**Figures S13-S15**) and characteristic values of interest (CMT, CMC, and D_H) are summarized in **Table 1**.

Table 1: *Summary of the CMT, CMC and D_H values (respectively at 80 µM, 37°C, and 50°C) for the library of HA-ELP bioconjugates. CMT: N = 3 except for * N = 4. CMC: N = 1. D_H: N = 4-8.*

	CMT at 80 µM (°C)			CMC at 37°C (µM)			D_H at 50°C (nm)		
Bioconjugate	**HA 4.6k**	**HA 24k**	**HA 42k**	**HA 4.6k**	**HA 24k**	**HA 42k**	**HA 4.6k**	**HA 24k**	**HA 42k**
ELP n60	**36** (± 1.6)*	**39.7** (± 2.1)	**42.3** (± 1.7)	**23**	**32**	**46**	**77** (± 25)	**117** (± 30)	**239** (± 38)
ELP n80	**31** (± 0.7)*	**34** (± 0.8)	**35.7** (± 0.5)	**35**	**24**	**32**	**48** (± 3)	**98** (± 9)	**182** (± 39)
ELP n100	**30.3** (± 1.2)	**31.3** (± 2.5)	**32.7** (± 0.9)	**18**	**25**	**28**	**60** (± 3)	**108** (± 9)	**194** (± 26)

Two tendencies were observed concerning the CMTs. The CMTs increased with the length of the HA segment and decreased with the length of the ELP segment. This result is fully consistent with the contribution of these two blocks to the general hydrophilicity of the system. A longer HA increases the hydrophilicity, leading to a higher CMT, while a longer ELP increases the hydrophobicity, leading to a lower CMT. These variations seem smaller for the largest ELP blocks, as well as the dependency with the concentration. (**Figure S12** panel **B)** At 80 µM, all the CMTs are comprised between 30°C-42°C, a perfectly suitable range of temperatures for forthcoming *in vitro* and *in vivo* biological studies where mild hypo- and hyperthermia shall be investigated. However, the influence of the bioconjugate's composition has to be considered: depending on the relative length of the two blocks, the system in physiological conditions can indeed be present either as coacervates (CMT>37°C) or as nanoparticles (CMT<37°C).

The hydrodynamic diameter (D_H) of nanoparticles were measured by DLS (z-average) at 50°C (highly enough above the CMT of all bioconjugates). (**Table 1**) The evolution of hydrodynamic diameters followed similar trends than the CMTs: the size of nanoparticles decreased with increasing ELP block length and with decreasing HA block length. Indeed, the deployment in surface of a longer hydrophilic HA logically increases the nanoparticle's size, while a longer and more hydrophobic ELP leads to a greater compaction of the core and to a smaller D_H. Noteworthy, the values for HA-ELPn60 bioconjugates are artificially increased by the presence of aggregates in the samples. For all $HA_{4.6k}$-ELP and HA_{24k}-ELP bioconjugates, the size of nanoparticles was far below 200 nm and thus fully compatible with systemic administrations and accumulation in tumor through the enhanced permeation and retention effect.

Concerning the CMC, the same tendency was observed with the increase of the HA block leading to a higher CMC. However, there is not obvious tendency with the evolution of ELP block size. The values are all comprised between 18-46 µM. An injection at such concentration could be contemplated *in vivo* in a murine model, but would be precluded in human, justifying further improvement of the system.

A deeper characterization of $HA_{4.6k}$-ELPn80 self-assembled nanoparticles was achieved using complementary techniques. (**Figure 6**)

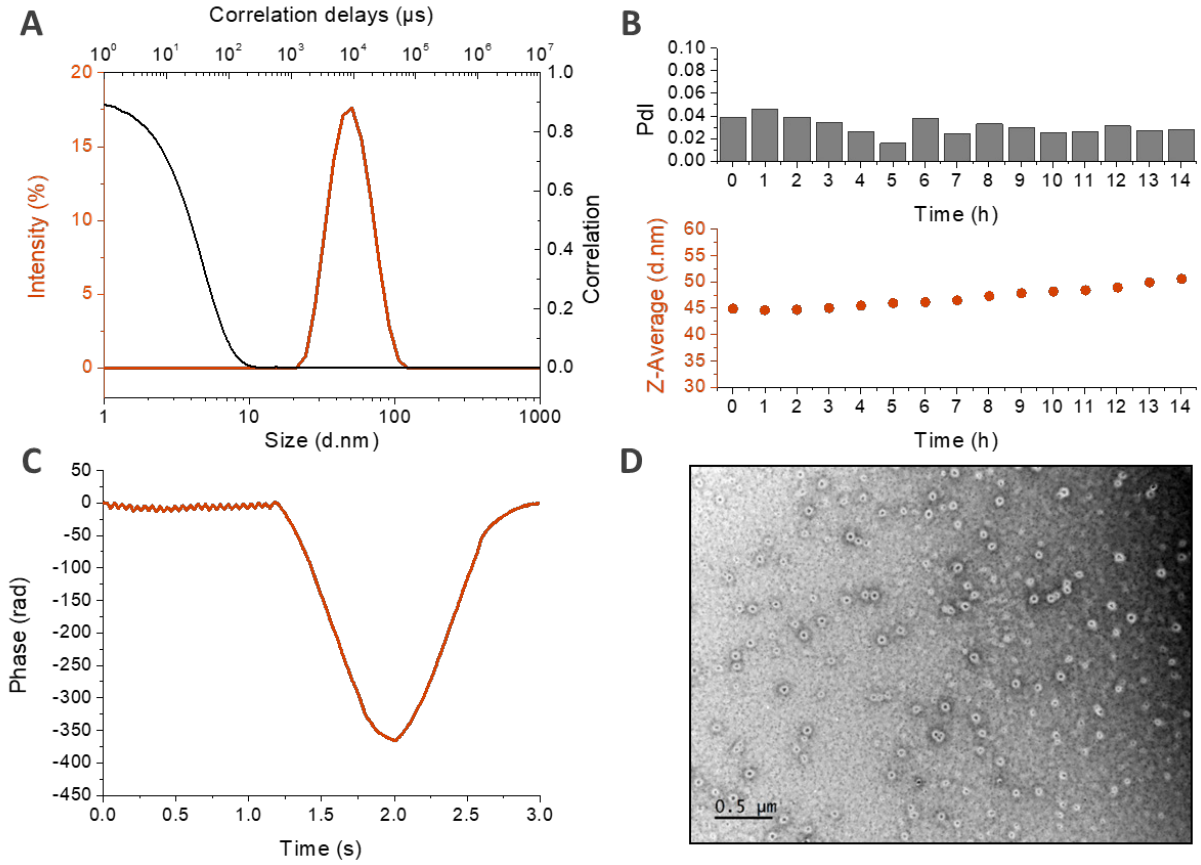

Figure 6: *Physicochemical characterization of the self-assembled nanoparticles based on $HA_{4,6k}$-ELPn80 bioconjugates. (A) Size distribution (in intensity) and correlogram from DLS analysis at 50°C (78 µM in PBS). (B) Stability over time at 37°C: evolution of the Z-Average and the PdI measured by DLS with time (78 µM in PBS). (C) Zeta Potential measurements (78 µM in HEPES buffer, 60°C). (D) TEM micrograph (2.6 µM in pure water, drop deposition at 80°C, samarium acetate staining).*

DLS measurements made in PBS at 80 µM are displayed in **Figure 6A** and **B**. In panel **A**, the size distribution in intensity at 50°C confirms the presence at high temperature of a unique population, with a narrow size dispersity centered around 40 nm. This population seems to be stable over time at 37°C, as shown in **Figure 6B**. If a slight increase of the z-average can be observed with time, the PdI keeps its low value, which demonstrates the maintenance of a low dispersity and the absence of destabilization. The structure of the nanoparticles was then investigated by zeta potential measurements in HEPES buffer at 60°C. (**Figure 6C)** The negative mean value suggests that the negatively charged HA is present at the surface of the nanoparticle, confirming a core-shell structure hypothesized earlier, with the hydrophobic ELP buried in the core and the hydrophilic HA deployed on the surface. Finally, the morphology of nanoparticles was assessed by transmission electronic microscopy (TEM). This time, the solution was prepared at lower concentration (2.6 µM) in pure

water in order to avoid the formation of salts crystals. **Figure 6D** reveals spherical objects with a regular shape and homogeneous size, around 100 nm. This value is higher than the D_H measured by DLS (**Figure 6B)** due to the difference in salinity of the solutions. In the absence of salts, the nanoparticles are more hydrated, which increases their size. This order of magnitude is however consistent with observations previously made for HA_{7k}-ELPn40 nanoparticles in pure water (200-300 nm at 52°C).[17]

CONCLUSION

We have herein described an optimized synthetic strategy to access a library of HA-*b*-ELP bioconjugates presenting a bioactive, CD44-targeting HA segment, and a thermo-responsive biocompatible polypeptide block. The bioconjugation reaction was performed by SPAAC in water, a catalyst-, co-reactant- and organic solvent-free synthetic process being desirable for subsequent biological/biomedical applications. The efficient isolation of the bioconjugates by a simple centrifugation above the CMT in water adds on to the straightforwardness of the process advantageous for a possible development at industrial scale. A thorough physico-chemical study of the nine HA-*b*-ELP bioconjugates was then performed in an attempt to investigate structure-property relationships. In particular, the determination of the critical conditions for thermally-driven self-assembly has been carried out upon temperature (CMT) and concentration (CMC) gradients, leading to a phase diagram for each of these bioconjugates. It has been observed that if the CMT values were fully compatible with *in vivo* applications, the CMCs were relatively high, indicating a compromised stability of nanoparticles upon dilution, and therefore a specific issue to address for subsequent biological studies. Some general rules on physico-chemical characteristics (CMT, CMC, D_H) versus macromolecular parameters could be established and found in agreement with previous studies: *i*) an increase in the HA length, causing an increase of the general hydrophilicity of the bioconjugate, lead to an increase in the CMT, CMC and D_H values; *ii*) the increase of the ELP block length reduces the CMT as well as the dependence of the CMT over molar concentration, but surprisingly reduces the size of nanoparticles conversely to our expectations.[5] Four of the bioconjugates ($HA_{4.6k}$-ELPn80 or n100 and HA_{24k}-ELPn80 or n100) were found to self-assemble into well-defined spherical core-shell nanoparticles, with a negative surface charge due to the HA block constituting the shell, a D_H comprised between 40-200 nm in physiological conditions and a good stability over time at 37°C.

ASSOCIATED CONTENT

Supporting information

Experimental procedures, characterization of ELPs, DBCO-ELP and HA-N_3, and additional characterizations of the self-assembly of all HA-*b*-ELP bioconjugates are available in the supporting information.

AUTHORS INFORMATIONS

Corresponding authors:

garanger@enscbp.fr and lecommandoux@enscbp.fr

Author contributions:

ML was involved in investigation, project administration, resources and writing of the first manuscript draft. YX was involved in resources ($HA_{4.6k}$-N_3). LD (SPAAC experiments) and LM (Nile Red experiments) were involved in investigation. EG and SL were involved in conceptualization, funding acquisition, project administration, and writing of the final manuscript. All authors have given approval to the final version of the manuscript.

CONFLICTS OF INTEREST

There are no conflicts to declare.

ACKNOWLEDGMENTS

Authors would like to thank Prof. Bertrand Garbay, Ms. Clara Toulouse, Ms. Chloé Ilos, and Ms. Pauline Coutand for their technical assistance in the recombinant production of the ELPs. The French Ministry for Higher Education and Research is gratefully acknowledged for the doctoral grant awarded to ML. China Scholarship Council and Université de Bordeaux (UB-CSC 2015) are acknowledged for the financial support to YX. This work was also supported by the French National Research Agency (ANR-15-CE07-0002). Continuous support from Univ. Bordeaux, CNRS and Bordeaux-INP is greatly acknowledged.

REFERENCES

(1) MacEwan, S. R.; Chilkoti, A. Applications of Elastin-like Polypeptides in Drug Delivery. *J. Controlled Release* **2014**, *190*, 314–330. https://doi.org/10.1016/j.jconrel.2014.06.028.

(2) Jenkins, I. C.; Milligan, J. J.; Chilkoti, A. Genetically Encoded Elastin-Like Polypeptides for Drug Delivery. *Adv. Healthc. Mater.* **2021**, 2100209. https://doi.org/10.1002/adhm.202100209.

(3) Guda, C.; Zhang, X.; McPherson, D. T.; Xu, J.; Cherry, J. H.; Urry, D. W.; Daniell, H. Hyper Expression of an Environmentally Friendly Synthetic Polymer Gene. *Biotechnol. Lett.* **1995**, *17* (7), 745–750. https://doi.org/10.1007/BF00130362.

(4) Roberts, S.; Dzuricky, M.; Chilkoti, A. Elastin-like Polypeptides as Models of Intrinsically Disordered Proteins. *FEBS Lett.* **2015**, *589* (19PartA), 2477–2486. https://doi.org/10.1016/j.febslet.2015.08.029.

(5) Garanger, E.; MacEwan, S. R.; Sandre, O.; Brûlet, A.; Bataille, L.; Chilkoti, A.; Lecommandoux, S. Structural Evolution of a Stimulus-Responsive Diblock Polypeptide Micelle by Temperature Tunable Compaction of Its Core. *Macromolecules* **2015**, *48* (18), 6617–6627. https://doi.org/10.1021/acs.macromol.5b01371.

(6) Rodríguez-Cabello, J. C.; Martín, L.; Alonso, M.; Arias, F. J.; Testera, A. M. "Recombinamers" as Advanced Materials for the Post-Oil Age. *Polymer* **2009**, *50* (22), 5159–5169. https://doi.org/10.1016/j.polymer.2009.08.032.

(7) McPherson, D. T.; Xu, J.; Urry, D. W. Product Purification by Reversible Phase Transition FollowingEscherichia ColiExpression of Genes Encoding up to 251 Repeats of the Elastomeric Pentapeptide GVGVP. *Protein Expr. Purif.* **1996**, *7* (1), 51–57. https://doi.org/10.1006/prep.1996.0008.

(8) Meyer, D. E.; Chilkoti, A. Protein Purification by Inverse Transition Cycling. In *Protein-Protein Interaction: A Molecular Cloning Manual*; **2002**, Chapter 18, 329–343.

(9) Urry, D. W.; Long, M. M.; Cox, B. A.; Ohnishi, T.; Mitchell, L. W.; Jacobs, M. The Synthetic Polypentapeptide of Elastin Coacervates and Forms Filamentous Aggregates. *Biochim. Biophys. Acta BBA - Protein Struct.* **1974**, *371* (2), 597–602. https://doi.org/10.1016/0005-2795(74)90057-9.

(10) Urry, D. W.; Luan, C. H.; Parker, T. M.; Gowda, D. C.; Prasad, K. U.; Reid, M. C.; Safavy, A. Temperature of Polypeptide Inverse Temperature Transition Depends on Mean Residue Hydrophobicity. *J. Am. Chem. Soc.* **1991**, *113* (11), 4346–4348. https://doi.org/10.1021/ja00011a057.

(11) MacKay, J. A.; Callahan, D. J.; FitzGerald, K. N.; Chilkoti, A. Quantitative Model of the Phase Behavior of Recombinant PH-Responsive Elastin-Like Polypeptides. *Biomacromolecules* **2010**, *11* (11), 2873–2879. https://doi.org/10.1021/bm100571j.

(12) Meyer, D. E.; Chilkoti, A. Quantification of the Effects of Chain Length and Concentration on the Thermal Behavior of Elastin-like Polypeptides. *Biomacromolecules* **2004**, *5* (3), 846–851. https://doi.org/10.1021/bm034215n.

(13) McDaniel, J. R.; Radford, D. C.; Chilkoti, A. A Unified Model for De Novo Design of Elastin-like Polypeptides with Tunable Inverse Transition Temperatures. *Biomacromolecules* **2013**, *14* (8), 2866–2872. https://doi.org/10.1021/bm4007166.

(14) Reguera, J.; Urry, D. W.; Parker, T. M.; McPherson, D. T.; Rodríguez-Cabello, J. C. Effect of NaCl on the Exothermic and Endothermic Components of the Inverse Temperature Transition of a Model Elastin-like Polymer. *Biomacromolecules* **2007**, *8* (2), 354–358. https://doi.org/10.1021/bm060936l.

(15) Cho, Y.; Zhang, Y.; Christensen, T.; Sagle, L. B.; Chilkoti, A.; Cremer, P. S. Effects of Hofmeister Anions on the Phase Transition Temperature of Elastin-like Polypeptides. *J. Phys. Chem. B* **2008**, *112* (44), 13765–13771. https://doi.org/10.1021/jp8062977.

(16) Saha, S.; Banskota, S.; Roberts, S.; Kirmani, N.; Chilkoti, A. Engineering the Architecture of Elastin-Like Polypeptides: From Unimers to Hierarchical Self-Assembly. *Adv. Ther.* **2020**, *3* (3), 1900164. https://doi.org/10.1002/adtp.201900164.

(17) Xiao, Y.; Chinoy, Z. S.; Pecastaings, G.; Bathany, K.; Garanger, E.; Lecommandoux, S. Design of Polysaccharide- *b* -Elastin-Like Polypeptide Bioconjugates and Their Thermoresponsive Self-Assembly. *Biomacromolecules* **2020**, *21* (1), 114–115. https://doi.org/10.1021/acs.biomac.9b01058.

(18) van Eldijk, M. B.; Smits, F. C. M.; Vermue, N.; Debets, M. F.; Schoffelen, S.; van Hest, J. C. M. Synthesis and Self-Assembly of Well-Defined Elastin-Like Polypeptide–Poly(Ethylene Glycol) Conjugates. *Biomacromolecules* **2014**, *15* (7), 2751–2759. https://doi.org/10.1021/bm5006195.

(19) Chen, T.-H. H.; Bae, Y.; Furgeson, D. Y.; Kwon, G. S. Biodegradable Hybrid Recombinant Block Copolymers for Non-Viral Gene Transfection. *Int. J. Pharm.* **2012**, *427* (1), 105–112. https://doi.org/10.1016/j.ijpharm.2011.09.035.

(20) Furgeson, D. Y.; Dreher, M. R.; Chilkoti, A. Structural Optimization of a "Smart" Doxorubicin–Polypeptide Conjugate for Thermally Targeted Delivery to Solid Tumors. *J. Controlled Release* **2006**, *110* (2), 362–369. https://doi.org/10.1016/j.jconrel.2005.10.006.

(21) Bhattacharyya, J.; Bellucci, J. J.; Weitzhandler, I.; McDaniel, J. R.; Spasojevic, I.; Li, X.; Lin, C.-C.; Chi, J.-T. A.; Chilkoti, A. A Paclitaxel-Loaded Recombinant Polypeptide Nanoparticle Outperforms Abraxane in Multiple Murine Cancer Models. *Nat. Commun.* **2015**, *6* (1), 7939. https://doi.org/10.1038/ncomms8939.

(22) Luginbuhl, K. M.; Mozhdehi, D.; Dzuricky, M.; Yousefpour, P.; Huang, F. C.; Mayne, N. R.; Buehne, K. L.; Chilkoti, A. Recombinant Synthesis of Hybrid Lipid–Peptide Polymer Fusions That Self-Assemble and Encapsulate Hydrophobic Drugs. *Angew. Chem. Int. Ed.* **2017**, *56* (45), 13979–13984. https://doi.org/10.1002/anie.201704625.

(23) Mozhdehi, D.; Luginbuhl, K. M.; Simon, J. R.; Dzuricky, M.; Berger, R.; Varol, H. S.; Huang, F. C.; Buehne, K. L.; Mayne, N. R.; Weitzhandler, I.; Bonn, M.; Parekh, S. H.; Chilkoti, A. Genetically Encoded Lipid–Polypeptide Hybrid Biomaterials That Exhibit Temperature-Triggered Hierarchical Self-Assembly. *Nat. Chem.* **2018**, *10* (5), 496–505. https://doi.org/10.1038/s41557-018-0005-z.

(24) Mozhdehi, D.; Luginbuhl, K. M.; Dzuricky, M.; Costa, S. A.; Xiong, S.; Huang, F. C.; Lewis, M. M.; Zelenetz, S. R.; Colby, C. D.; Chilkoti, A. Genetically Encoded Cholesterol-Modified Polypeptides. *J. Am. Chem. Soc.* **2019**, *141* (2), 945–951. https://doi.org/10.1021/jacs.8b10687.

(25) Le Fer, G.; Portes, D.; Goudounet, G.; Guigner, J.-M.; Garanger, E.; Lecommandoux, S. Design and Self-Assembly of PBLG- b -ELP Hybrid Diblock Copolymers Based on Synthetic and Elastin-like Polypeptides. *Org. Biomol. Chem.* **2017**, *15* (47), 10095–10104. https://doi.org/10.1039/C7OB01945A.

(26) Lee, T. a. T.; Cooper, A.; Apkarian, R. P.; Conticello, V. P. Thermo-Reversible Self-Assembly of Nanoparticles Derived from Elastin-Mimetic Polypeptides. *Adv. Mater.* **2000**, *12* (15), 1105–1110. https://doi.org/10.1002/1521-4095(200008)12:15<1105::AID-ADMA1105>3.0.CO;2-1.

(27) Hassouneh, W.; Zhulina, E. B.; Chilkoti, A.; Rubinstein, M. Elastin-like Polypeptide Diblock Copolymers Self-Assemble into Weak Micelles. *Macromolecules* **2015**, *48* (12), 4183–4195. https://doi.org/10.1021/acs.macromol.5b00431.

(28) Janib, S. M.; Pastuszka, M. F.; Aluri, S.; Folchman-Wagner, Z.; Hsueh, P. Y.; Shi, P.; Lin, Y. A.; Cui, H.; MacKay, J. A. A Quantitative Recipe for Engineering Protein Polymer Nanoparticles. *Polym. Chem.* **2014**, *5* (5), 1614–1625. https://doi.org/10.1039/C3PY00537B.

(29) Widder, K.; R. MacEwan, S.; Garanger, E.; Núñez, V.; Lecommandoux, S.; Chilkoti, A.; Hinderberger, D. Characterisation of Hydration and Nanophase Separation during the Temperature Response in Hydrophobic/Hydrophilic Elastin-like Polypeptide (ELP) Diblock Copolymers. *Soft Matter* **2017**, *13* (9), 1816–1822. https://doi.org/10.1039/C6SM02427K.

(30) Weitzhandler, I.; Dzuricky, M.; Hoffmann, I.; Garcia Quiroz, F.; Gradzielski, M.; Chilkoti, A. Micellar Self-Assembly of Recombinant Resilin-/Elastin-Like Block Copolypeptides. *Biomacromolecules* **2017**, *18* (8), 2419–2426. https://doi.org/10.1021/acs.biomac.7b00589.

(31) Smits, F. C. M.; Buddingh, B. C.; van Eldijk, M. B.; van Hest, J. C. M. Elastin-Like Polypeptide Based Nanoparticles: Design Rationale Toward Nanomedicine: Elastin-Like Polypeptide Based Nanoparticles: Design Rationale Toward Nanomedicine. *Macromol. Biosci.* **2015**, *15* (1), 36–51. https://doi.org/10.1002/mabi.201400419.

(32) MacEwan, S. R.; Chilkoti, A. Elastin-like Polypeptides: Biomedical Applications of Tunable Biopolymers. *Pept. Sci.* **2010**, *94* (1), 60–77. https://doi.org/10.1002/bip.21327.

(33) Varanko, A. K.; Su, J. C.; Chilkoti, A. Elastin-Like Polypeptides for Biomedical Applications. *Annu. Rev. Biomed. Eng.* **2020**, *22* (1), 343–369. https://doi.org/10.1146/annurev-bioeng-092419-061127.

(34) Georgilis, E.; Abdelghani, M.; Pille, J.; Aydinlioglu, E.; van Hest, J. C. M.; Lecommandoux, S.; Garanger, E. Nanoparticles Based on Natural, Engineered or Synthetic Proteins and Polypeptides for Drug Delivery Applications. *Int. J. Pharm.* **2020**, *586*, 119537. https://doi.org/10.1016/j.ijpharm.2020.119537.

(35) Shi, P.; Aluri, S.; Lin, Y.-A.; Shah, M.; Edman, M.; Dhandhukia, J.; Cui, H.; MacKay, J. A. Elastin-Based Protein Polymer Nanoparticles Carrying Drug at Both Corona and Core Suppress Tumor Growth in Vivo. *J. Controlled Release* **2013**, *171* (3), 330–338. https://doi.org/10.1016/j.jconrel.2013.05.013.

(36) Costa, S. A.; Mozhdehi, D.; Dzuricky, M. J.; Isaacs, F. J.; Brustad, E. M.; Chilkoti, A. Active Targeting of Cancer Cells by Nanobody Decorated Polypeptide Micelle with Bio-Orthogonally Conjugated Drug. *Nano Lett.* **2019**, *19* (1), 247–254. https://doi.org/10.1021/acs.nanolett.8b03837.

(37) Bidwell, G. L.; Raucher, D. Application of Thermally Responsive Polypeptides Directed against C-Myc Transcriptional Function for Cancer Therapy. *Mol. Cancer Ther.* **2005**, *4* (7), 1076–1085. https://doi.org/10.1158/1535-7163.MCT-04-0253.

(38) Sarangthem, V.; Kim, Y.; Singh, T. D.; Seo, B.-Y.; Cheon, S.-H.; Lee, Y.-J.; Lee, B.-H.; Park, R.-W. Multivalent Targeting Based Delivery of Therapeutic Peptide Using AP1-ELP Carrier for Effective Cancer Therapy. *Theranostics* **2016**, *6* (12), 2235–2249. https://doi.org/10.7150/thno.16425.

(39) Zhang, W.; Garg, S.; Eldi, P.; Zhou, F. H.; Johnson, I. R. D.; Brooks, D. A.; Lam, F.; Rychkov, G.; Hayball, J.; Albrecht, H. Targeting Prostate Cancer Cells with Genetically Engineered Polypeptide-Based Micelles Displaying Gastrin-Releasing Peptide. *Int. J. Pharm.* **2016**, *513* (1), 270–279. https://doi.org/10.1016/j.ijpharm.2016.09.039.

(40) Sun, M.; Guo, J.; Hao, H.; Tong, T.; Wang, K.; Gao, W. Tumour-Homing Chimeric Polypeptide-Conjugated Polypyrrole Nanoparticles for Imaging-Guided Synergistic Photothermal and Chemical Therapy of Cancer. *Theranostics* **2018**, *8* (10), 2634–2645. https://doi.org/10.7150/thno.24705.

(41) Aluri, S. R.; Shi, P.; Gustafson, J. A.; Wang, W.; Lin, Y.-A.; Cui, H.; Liu, S.; Conti, P. S.; Li, Z.; Hu, P.; Epstein, A. L.; MacKay, J. A. A Hybrid Protein–Polymer Nanoworm Potentiates Apoptosis Better than a Monoclonal Antibody. *ACS Nano* **2014**, *8* (3), 2064–2076. https://doi.org/10.1021/nn403973g.

(42) Fluegel, S.; Buehler, J.; Fischer, K.; McDaniel, J. R.; Chilkoti, A.; Schmidt, M. Self-Assembly of Monodisperse Oligonucleotide-Elastin Block Copolymers into Stars and Compound Micelles. *Chem. - Eur. J.* **2011**, *17* (20), 5503–5506. https://doi.org/10.1002/chem.201100436.

(43) Dreher, M. R.; Simnick, A. J.; Fischer, K.; Smith, R. J.; Patel, A.; Schmidt, M.; Chilkoti, A. Temperature Triggered Self-Assembly of Polypeptides into Multivalent Spherical Micelles. *J. Am. Chem. Soc.* **2008**, *130* (2), 687–694. https://doi.org/10.1021/ja0764862.

(44) Pille, J.; van Lith, S. A. M.; van Hest, J. C. M.; Leenders, W. P. J. Self-Assembling VHH-Elastin-Like Peptides for Photodynamic Nanomedicine. *Biomacromolecules* **2017**, *18* (4), 1302–1310. https://doi.org/10.1021/acs.biomac.7b00064.

(45) Necas, J.; Bartosikova, L.; Brauner, P.; Kolar, J. Hyaluronic Acid (Hyaluronan): A Review. *Veterinární Medicína* **2008**, *53* (No. 8), 397–411. https://doi.org/10.17221/1930-VETMED.

(46) Mattheolabakis, G.; Milane, L.; Singh, A.; Amiji, M. M. Hyaluronic Acid Targeting of CD44 for Cancer Therapy: From Receptor Biology to Nanomedicine. *J. Drug Target.* **2015**, *23* (7–8), 605–618. https://doi.org/10.3109/1061186X.2015.1052072.

(47) Liu, A. Y. Expression of CD44 in Prostate Cancer Cells. *Cancer Lett.* **1994**, *76* (1), 63–69. https://doi.org/10.1016/0304-3835(94)90135-X.

(48) Penno, M. B.; August, J. T.; Baylin, S. B.; Mabry, M.; Linnoila, R. I.; Lee, V. S.; Croteau, D.; Yang, X. L.; Rosada, C. Expression of CD44 in Human Lung Tumors. *Cancer Res.* **1994**, *54* (5), 1381–1387.

(49) Kopp, R.; Fichter, M.; Schalhorn, G.; Danescu, J.; Classen, S. Frequent Expression of the High Molecular, 673-Bp CD44v3,v8-10 Variant in Colorectal Adenomas and Carcinomas. *Int. J. Mol. Med.* **2009**, *24* (5), 677–683. https://doi.org/10.3892/ijmm_00000279.

(50) Olsson, E.; Honeth, G.; Bendahl, P.-O.; Saal, L. H.; Gruvberger-Saal, S.; Ringnér, M.; Vallon-Christersson, J.; Jönsson, G.; Holm, K.; Lövgren, K.; Fernö, M.; Grabau, D.; Borg, Å.; Hegardt, C. CD44 Isoforms Are Heterogeneously Expressed in Breast Cancer and Correlate with Tumor Subtypes and Cancer Stem Cell Markers. *BMC Cancer* **2011**, *11* (1), 418. https://doi.org/10.1186/1471-2407-11-418.

(51) Chen, Y.; Fu, Z.; Xu, S.; Xu, Y.; Xu, P. The Prognostic Value of CD44 Expression in Gastric Cancer: A Meta-Analysis. *Biomed. Pharmacother.* **2014**, *68* (6), 693–697. https://doi.org/10.1016/j.biopha.2014.08.001.

(52) Li, X.-P.; Zhang, X.-W.; Zheng, L.-Z.; Guo, W.-J. Expression of CD44 in Pancreatic Cancer and Its Significance. *Int. J. Clin. Exp. Pathol.* **2015**, *8* (6), 6724–6731.

(53) Al-Hajj, M.; Wicha, M. S.; Benito-Hernandez, A.; Morrison, S. J.; Clarke, M. F. Prospective Identification of Tumorigenic Breast Cancer Cells. *Proc. Natl. Acad. Sci.* **2003**, *100* (7), 3983–3988. https://doi.org/10.1073/pnas.0530291100.

(54) Al-Hajj, M.; Becker, M. W.; Wicha, M.; Weissman, I.; Clarke, M. F. Therapeutic Implications of Cancer Stem Cells. *Curr. Opin. Genet. Dev.* **2004**, *14* (1), 43–47. https://doi.org/10.1016/j.gde.2003.11.007.

(55) Idowu, M. O.; Kmieciak, M.; Dumur, C.; Burton, R. S.; Grimes, M. M.; Powers, C. N.; Manjili, M. H. CD44+/CD24−/Low Cancer Stem/Progenitor Cells Are More Abundant in Triple-Negative Invasive Breast Carcinoma Phenotype and Are Associated with Poor Outcome. *Hum. Pathol.* **2012**, *43* (3), 364–373. https://doi.org/10.1016/j.humpath.2011.05.005.

(56) Orian-Rousseau, V. CD44 Acts as a Signaling Platform Controlling Tumor Progression and Metastasis. *Front. Immunol.* **2015**, *6*. https://doi.org/10.3389/fimmu.2015.00154.

(57) Prince, M. E.; Sivanandan, R.; Kaczorowski, A.; Wolf, G. T.; Kaplan, M. J.; Dalerba, P.; Weissman, I. L.; Clarke, M. F.; Ailles, L. E. Identification of a Subpopulation of Cells with Cancer Stem Cell Properties in Head and Neck Squamous Cell Carcinoma. *Proc. Natl. Acad. Sci.* **2007**, *104* (3), 973–978. https://doi.org/10.1073/pnas.0610117104.

(58) Najafi, M.; Farhood, B.; Mortezaee, K. Cancer Stem Cells (CSCs) in Cancer Progression and Therapy. *J. Cell. Physiol.* **2019**, *234* (6), 8381–8395. https://doi.org/10.1002/jcp.27740.

(59) Aruffo, A.; Stamenkovic, I.; Melnick, M.; Underhill, C. B.; Seed, B. CD44 Is the Principal Cell Surface Receptor for Hyaluronate. *Cell* **1990**, *61* (7), 1303–1313. https://doi.org/10.1016/0092-8674(90)90694-A.

(60) Dosio, F.; Arpicco, S.; Stella, B.; Fattal, E. Hyaluronic Acid for Anticancer Drug and Nucleic Acid Delivery. *Adv. Drug Deliv. Rev.* **2016**, *97*, 204–236. https://doi.org/10.1016/j.addr.2015.11.011.

(61) Lee, S. Y.; Kang, M. S.; Jeong, W. Y.; Han, D.-W.; Kim, K. S. Hyaluronic Acid-Based Theranostic Nanomedicines for Targeted Cancer Therapy. *Cancers* **2020**, *12* (4), 940. https://doi.org/10.3390/cancers12040940.

(62) Robert, L. Hyaluronan, a Truly "Youthful" Polysaccharide. Its Medical Applications. *Pathol. Biol.* **2015**, *63* (1), 32–34. https://doi.org/10.1016/j.patbio.2014.05.019.

(63) Stern, R.; Maibach, H. I. Hyaluronan in Skin: Aspects of Aging and Its Pharmacologic Modulation. *Clin. Dermatol.* **2008**, *26* (2), 106–122. https://doi.org/10.1016/j.clindermatol.2007.09.013.

(64) Pharmacopée Hyaluronate de Sodium.

(65) Dai, M.; Georgilis, E.; Goudounet, G.; Garbay, B.; Pille, J.; van Hest, J. C. M.; Schultze, X.; Garanger, E.; Lecommandoux, S. Refining the Design of Diblock Elastin-Like Polypeptides for Self-Assembly into Nanoparticles. *Polymers* **2021**, *13* (9), 1470. https://doi.org/10.3390/polym13091470.

(66) Agard, N. J.; Prescher, J. A.; Bertozzi, C. R. A Strain-Promoted [3 + 2] Azide−Alkyne Cycloaddition for Covalent Modification of Biomolecules in Living Systems. *J. Am. Chem. Soc.* **2004**, *126* (46), 15046–15047. https://doi.org/10.1021/ja044996f.

(67) Seitz, G.; Pohl, L.; Pohlke, R. 5,6-Didehydro-11,12-Dihydrodibenzo[a,e]-Cyclooctene. *Angew. Chem. Int. Ed. Engl.* **1969**, *8* (6), 447–448. https://doi.org/10.1002/anie.196904471.

(68) Kuzmin, A.; Poloukhtine, A.; Wolfert, M. A.; Popik, V. V. Surface Functionalization Using Catalyst-Free Azide−Alkyne Cycloaddition. *Bioconjug. Chem.* **2010**, *21* (11), 2076–2085. https://doi.org/10.1021/bc100306u.

(69) Munneke, S.; Prevost, J. R. C.; Painter, G. F.; Stocker, B. L.; Timmer, M. S. M. The Rapid and Facile Synthesis of Oxyamine Linkers for the Preparation of Hydrolytically Stable Glycoconjugates. *Org. Lett.* **2015**, *17* (3), 624–627. https://doi.org/10.1021/ol503634j.

(70) Duan, H.; Donovan, M.; Foucher, A.; Schultze, X.; Lecommandoux, S. Multivalent and Multifunctional Polysaccharide-Based Particles for Controlled Receptor Recognition. *Sci. Rep.* **2018**, *8* (1), 14730. https://doi.org/10.1038/s41598-018-32994-y.

(71) Spectrofluorometric Studies of the Lipid Probe, Nile Red. *J. Lipid Res.* **1985**, *26* (7), 781–789. https://doi.org/10.1016/S0022-2275(20)34307-8.

(72) Kurniasih, I. N.; Liang, H.; Mohr, P. C.; Khot, G.; Rabe, J. P.; Mohr, A. Nile Red Dye in Aqueous Surfactant and Micellar Solution. *Langmuir* **2015**, *31* (9), 2639–2648. https://doi.org/10.1021/la504378m.

(73) Sarkar, N.; Das, K.; Nath, D. N.; Bhattacharyya, K. Twisted Charge Transfer Processes of Nile Red in Homogeneous Solutions and in Faujasite Zeolite. *Langmuir* **1994**, *10* (1), 326–329. https://doi.org/10.1021/la00013a048.

(74) Greenspan, P.; Mayer, E. P.; Fowler, S. D. Nile Red: A Selective Fluorescent Stain for Intracellular Lipid Droplets. *J. Cell Biol.* **1985**, *100* (3), 965–973. https://doi.org/10.1083/jcb.100.3.965.

(75) Goodwin, A. P.; Mynar, J. L.; Ma, Y.; Fleming, G. R.; Fréchet, J. M. J. Synthetic Micelle Sensitive to IR Light via a Two-Photon Process. *J. Am. Chem. Soc.* **2005**, *127* (28), 9952–9953. https://doi.org/10.1021/ja0523035.

(76) Stuart, M. C. A.; van de Pas, J. C.; Engberts, J. B. F. N. The Use of Nile Red to Monitor the Aggregation Behavior in Ternary Surfactant–Water–Organic Solvent Systems. *J. Phys. Org. Chem.* **2005**, *18* (9), 929–934. https://doi.org/10.1002/poc.919.

Author manuscript of article published in *Biomaterials Science*, https://doi.org/10.1039/D2BM01149B

Aqueous synthesis and self-assembly of bioactive and thermo-responsive HA-*b*-ELP bioconjugates

Manon Levêque,[a] Ye Xiao,[a] Laura Durand,[a] Louise Massé,[a] Elisabeth Garanger,*[a] and Sébastien Lecommandoux*[a]

[a] Université de Bordeaux, CNRS, Bordeaux INP, LCPO, UMR 5629, Pessac F-33600, France.

EXPERIMENTAL SECTION

Materials

Starting biomacromolecules: Sodium hyaluronate (HA 5K, 20K, and 40K) were purchased from Lifecore Biomedical. For each size, the same batch was used for all the experiments, with precise molar masses of 4.6 kD, 24 kD, and 42 kD respectively. ELP[M_1V_3-n] with n = 60, 80, and 100 (*i.e.*, ELPn60, ELPn80 and ELPn100) were produced following previously reported procedures.[1]

Solvents: Ethanol (96.0%, EtOH), methanol (98.5%, MeOH), dimethylformamide (DMF, 99%), acetonitrile (99.9%, ACN), diethyl ether, and tetrahydrofuran (THF) were purchased from VWR and used as received. D_2O was provided by Eurisotop. Ultrapure water (18 MΩ-cm) was obtained by using a Millipore Milli-Q Biocel A10 purification unit.

Reactants: Acetic acid (AcOH, 99.8%), sodium cyanoborohyde (NaBH3CN, 95%), 3-Azido-1-propanamine (90%), sinapic acid, and Trizma® were purchased from Sigma-Aldrich. *N,N* Diisopropylethylamine (DIPEA,99%), sodium L- (AcONa, 99%), trifluoroacetic acid (TFA) , sodium nitrate (NaNO3) were acquired from Alfa Aesar. Ammonium acetate and sodium hydroxide (NaOH) were purchased from Fisher Scientific (FR), sodium hydrogenophosphate (Na_2HPO_4) from VWR, and DBCO-C6-NHS ester (DBCO) from Lumiprobe.

Synthesis

Saline buffers preparation

Saline TRIS buffer (TRISs) was prepared with 0.05 M Trisma-HCl (Trizma) and 0.15 M NaCl in ultrapure water. pH was adjusted to 7.4 with a 0.1M NaOH solution.

[1] Dai, M.; Georgilis, E.; Goudounet, G.; Garbay, B.; Pille, J.; van Hest, J.C.M.; Schultze, X.; Garanger, E.; Lecommandoux, S. Refining the Design of Diblock Elastin-Like Polypeptides for Self-Assembly into Nanoparticles. *Polymers* **2021**,*13*,1470. https:// doi.org/10.3390/polym13091470

PBS buffer was prepared by dilution of a 10X PBS commercial solution (*Euromedex*) at pH 7.0. Salinity was adjusted at 300 mosm with concentrated PBS and pH increased at 7.4 with a 0.1M NaOH solution.

Synthesis of hyaluronan-azide (HA-N_3)

Hyaluronan $HA_{4.6k}$ (500 mg, 110 µmol, 1 eq.) was dissolved in 3 mL of acetate buffer (AcONa/AcOH, 2M, pH 5,5) at 50°C. After addition of *N*-(3-azidopropyl)-*O*-methylhydroxylamine (390 mg, 3 mmol, 30 eq) and sodium cyanoborohydride (62.84 mg, 1 mmol, 10 eq), the solution was let under stirring at 50°C for 5 days (Thermomixer, 600 rpm). It was then purified by dialysis (1 kD pores membrane). The first 2 baths were done against a mixture of H2O/EtOH (1:1), and the next 4 against ultrapure water. After freeze-drying, the final product is a brittle white solid. Mass yield $r_{HA4.6k}$ = 84% (N=2).

A similar procedure has been followed for the functionalization of HA_{24k} and HA_{42k}, except for the use of a 3-Azido-1-propanamine as azide linker (commercially available) and smaller quantities: 100 mg of HA, and 20 equivalents of 3-Azido-1-propanamine and $NaBH_3CN$. Mean mass yield are respectively r_{HA24k} = 86% (N=3) and r_{HA42k} = 82% (N=5)

Synthesis of ELP-DBCO

ELPn80 (200 mg, 5.93 µmol, 1 eq.) was dissolved in 2 mL DMF under inert atmosphere (Ar). DIPEA was added (3.07 mg, 23.74 µmol, 4 eq.), followed by DBCO-C6-NHS ester (12.8 mg, 29.67 µmol, 5 eq.). The reactive medium was let stirring under inert atmosphere and shielded from light at room temperature for 2 days. Purification was carried out by precipitation in cold diethyl ether. ELP was then retrieved in the pellet after centrifugation at low temperature and dissolved again in cold ultrapure water. The solution was dialysed (3.5 kD pores membrane) against ultrapure water during 1-4 days (6 baths). Final product obtained after freeze-drying was a white fluffy solid. Mean mass yield r_{ELPn80} = 85% (N=8). A similar procedure was applied to the functionalization of ELPn60 and ELPn100 with respective mean mass yields of r_{ELPn60} = 87% (N=2) and $r_{ELPn100}$ = 91% (N=5).

Synthesis of HA-ELP bioconjugates (SPAAC)

DBCO-ELPn80 (20 mg, 0.59 µmol, 1 eq.) and $HA_{4.6k}$-N_3 (1.37 mg, 0.29 µmol, 0.5 eq.) were separately dissolved in 500 µL of ultrapure water, and mixed together. The 1 mL solution was then put under inert atmosphere (argon) and let stirring at 4°C for 2 days. The purification was achieved by centrifugation at high temperature: 5 min heating of the solution with a ThermomixerTM Eppendorf (*ThermoFisher Scientific*) followed by a 5 min centrifugation at 35°C and 10,000g. The supernatant containing the HA-ELP bioconjugates was then separated from the pellet containing the DBCO-ELP in excess. After freeze-drying, the final product is a white fluffy solid. The mean mass yield is $r_{HA4.6k\text{-}ELPn80}$ = 95% and the mean reaction yield η = 78% (N=12). The same protocol was applied to the

synthesis of all the 9 bioconjugates of the library. The mean reaction yields are displayed in the Table below.

Mass yield = total final mass (bioconjugates + DBCO in excess) / initial reactant mass x 100
Reaction yield = dry supernatant mass (bioconjugates only) / theoretical mass (if 100% conversion) x 100

Table S2: Mean reaction yields for the synthesis of the HA-ELP bioconjugates library by SPAAC

Reaction yield (%)	HA		
ELP	HA 4.6k	HA 24k	HA 42k
ELP n60	**84%** ± 19 (N=4)	**74%** ± 17 (N=4)	**95%** ± 3 (N=3)
ELP n80	**78%** ± 10 (N=12)	**62%** ± 11 (N=6)	**71%** ± 13 (N=7)
ELP n100	**80%** ± 12 (N=6)	**55%** ± 6 (N=5)	**78%** ± 12 (N=5)

Recycling:

The DBCO-ELPn80 in excess present in the pellet was re-dissolved in 1 mL of ultrapure water and freeze dried. It was then used again in a new SPAAC reaction following the protocol described above. For $HA_{4.6k}$-ELPn80 synthesis with recycled DBCO-ELPn80 the mass yield was $r_{HA4.6k\text{-}ELPn80}$ = 91% and the reaction yield η = 39% (N=2).

Characterization

Gel electrophoresis

Electrophoresis analysis were carried on SDS-PAGE gels (*BioRad MiniPROTEAN TGX, non-stained, gradient 4%-20%*), on samples taken in the medium before purification (b.p.) and after centrifugation at 35°C for 5 min in the supernatant (sup) and the pellet (pel). The samples were prepared by dilution in deionized water by a ratio 1/5 (b.p.), 3/10 (sup) and 1/10 (pel), and addition of Laemmli buffer (*Biorad*). The electrophoresis was carried on a volume of 10 µL in each lane, in a Tris/Glycine/SDS buffer (*Biorad*), with a BioRad MiniPROTEAN® Tetra System device. The tension was kept constant at 300 mV and the intensity has been fixed at 25 mA per gel for 45 min. After rinse the gel was imaged with a BioRad GelDoc™ EZ Imager.

Nuclear Magnetic resonance analysis (NMR)

^{1}H NMR, ^{13}C NMR, HSQC and COSY spectra were acquired at 277K (4°C) on a Bruker Advance NEO 400 spectrometer equipped with a cryo-probe (multinuclear z-gradient direct cryoprobe-head,

5mm, *Bruker*), and at 298K (25°C) on a Bruker AVANCE III HD-400 spectrometer. Both work at 400.3 MHz.

Samples were prepared from freeze-dried compounds by their dissolution at 8 mg/mL in 400 µL of D_2O *(Eurisotop)*. The solvent peak was selected as reference (δ = 4.69 ppm at 277 K) and the spectra processed on TopSpin software.

Size exclusion chromatography

The SEC analysis were performed on an Ultimate 3000 device (*Thermoscientific*®) equipped with triple detection: it includes a diode array detector (DAD), a multi-angles light scattering detector (MALS, 18 angles), and a differential refractive index detector (dRI) from Wyatt technology. The eluent was a phosphate buffer (0.1M $NaNO_3$; 0.05M HPO_4^{2-}; pH 9). The samples were prepared in this buffer at a concentration of 2 mg/mL, with ethylene glycol as flow marker. The compounds were separated on Shodex OH Pack KD columns: a first SB G (guard 6*40) followed by two SB 804 HQ (8 * 300) with size exclusion of 5 x 10^3 – 4 x 10^5 g/mol. Measurements were performed at a flowrate of 0.6 mL/min at a pressure of 50 bar and columns temperature was held at 26°C.

For the ELPs alone, the eluent was a mixture of acetonitrile (ACN, 35%) and aqueous buffer (65%) of acetic acid (0.3M) and ammonium acetate (0.2M). The samples were prepared in this buffer at a concentration of 2 mg/mL, with ethylene glycol as flow marker. The separation was done on two TOSOH columns (7.8 * 300) with respective size exclusion < 10^6 g/mol and < 2 x 10^5 g/mol.

Data were processed on Astra software and molar masses were calculated with the dn/dC value of 0.1391 previously measured for ELPn40.

Mass spectrometry (MALDI)

Mass scpetrometry analysis were performed at the CESAMO analysis platform of the Institute of Molecular Sciences (ISM, UMR 5255). They were done by matrix-assisted laser desorption/ionization (MALDI) on a MALDI-TOF (*Autoflex maX TOF, Brucker Daltonics*) spectrometer equipped with a SMART-bean II (Nd:YAG, 355 nm) laser.

The samples were prepared by dissolution of the freeze-dried compounds in a mixture H_2O/ACN (1:1) at a concentration of 10 mg/mL. The matrix is a solution of sinapic acid at 10 mg/mL in H_2O/ACN (1:1) with TFA 0.1%. The final solution was obtained by mixing the sample solution with the matrix in a 1:9 volume ratio. A drop of 1.5 µL was deposited on an analysis plate and let to dry. The deposit and analysis were done in duplicate. Measurements were done in positive linear mode without calibration. A measurement of the compound before functionalization is systematically done to serve as reference.

Dynamic Light Scattering Measurements (DLS)

Dynamic light scattering measurements were performed on NanoZS instrument (*Malvern*, λ = 633 nm) at a 173° angle at a constant position in the cuvette (constant scattering volume). Quartz cuvettes were used (*Hellma Analytics High Precision Cell with Quartz SUPRASIL,* optical path 3x3 mm) for a volume of 70 µL. The solutions of bioconjugates were prepared in PBS (300 mosm, pH 7.4) at 78 µM. Precise z-average values and size distributions were recorded at temperature below (4-5°C) or above (40-50°C) CMT. The automatic mode recorded 3 measurements of 13-16 runs of 10s. The evolutions of derived count rate (DCR) and z-average with temperature were plotted during a heating ramp or cycles of heating-cooling ramps. 3 measurements of 3 runs of 10s were recorded every 2°C.

Stability of the nanoparticles over time was assessed by DLS measurement of a solution of $HA_{4.6k}$-ELPn80 at 78 µM in PBS (300 mosm, pH 7.4) kept at 37°C. One measurement of 13-16 runs of 10s was done every 1h for 14h.

Zeta potential measurements

Zeta potential measurements were done on a Zetasizer Ultra device (Malvern Panalytical) in corresponding cells (Zetasizer Nano Series, DTS1070, Malvern) using the diffusion barrier method. A solution of $HA_{4.6k}$-ELPn80 bioconjugate was prepared at 26 µM in an HEPES buffer (20 mM). The analysis cell was filled with 1 mL of this same buffer. A volume of 100 µL of sample solution was then slowly injected at the bottom of the cell and 3 measurement of 3 sec. performed at 60°C. The first period (0-1.25 sec.) correspond to the Fast Field Reversal (FFR) mode and the second one (1.25-3 sec.) to the Slow Field Reversal (SFR) mode giving access to the mean value of zeta potential and distribution, respectively.

Transmission Electron Microscopy (TEM)

The TEM imaging was performed at the Bordeaux Imaging Center (BIC) on a Hitachi H7650 microscope (80 kV) equipped with a SC1000 ORIUS 11 Mpx (*GATAN*) camera.

The sample of nanoparticles of $HA_{4,6k}$-ELPn80 was prepared at 76 µM (1 mg/mL) in ultra-ultrapure water. The solution was heated at 70°C for 5 min and 5 µL were dropped on a carbon grid at 80°C and let to dry for 1 min. The stain was done by the addition of 5 µL of samarium acetate (*Sigma Aldrich*) in solution at 20 mg/mL heated at 70°C and let to dry for 1 min.

SUPPLEMENTARY FIGURES

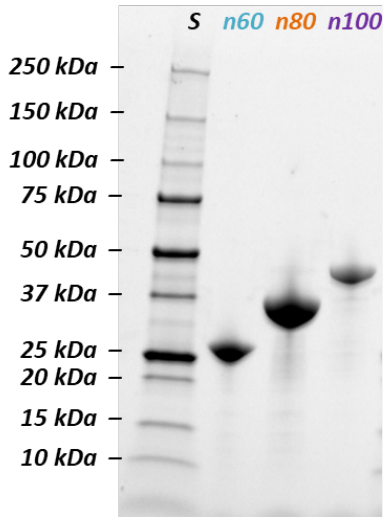

Figure S1: *SDS-PAGE analysis of the recombinant ELP[M_1V_3-n] (n = 60, 80, 100). S: Protein size markers.*

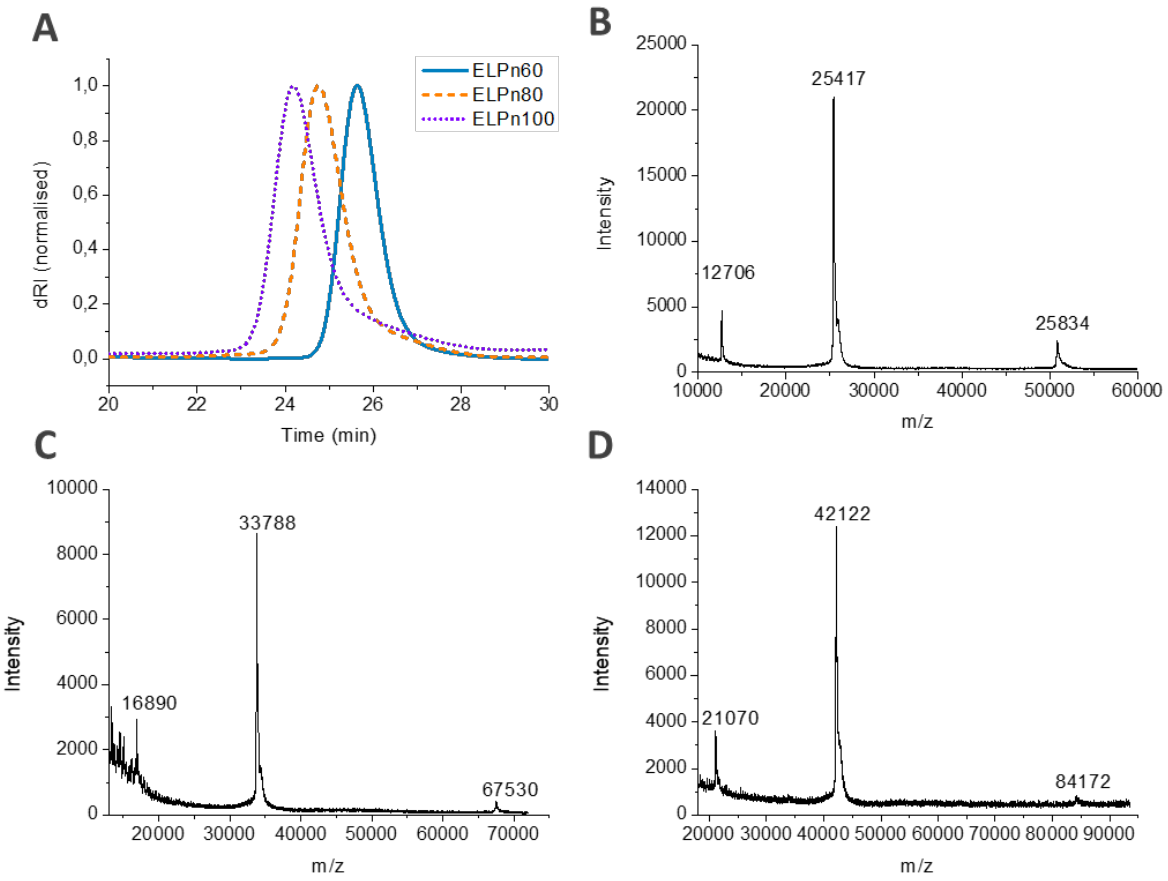

Figure S2: *(A) Size exclusion chromatograms of the ELP[M_1V_3-n] (n = 60, 80, 100), ammonium acetate buffer; (B-D) MALDI mass spectra of ELPn60 (B), ELPn80 (C), ELPn100 (D).*

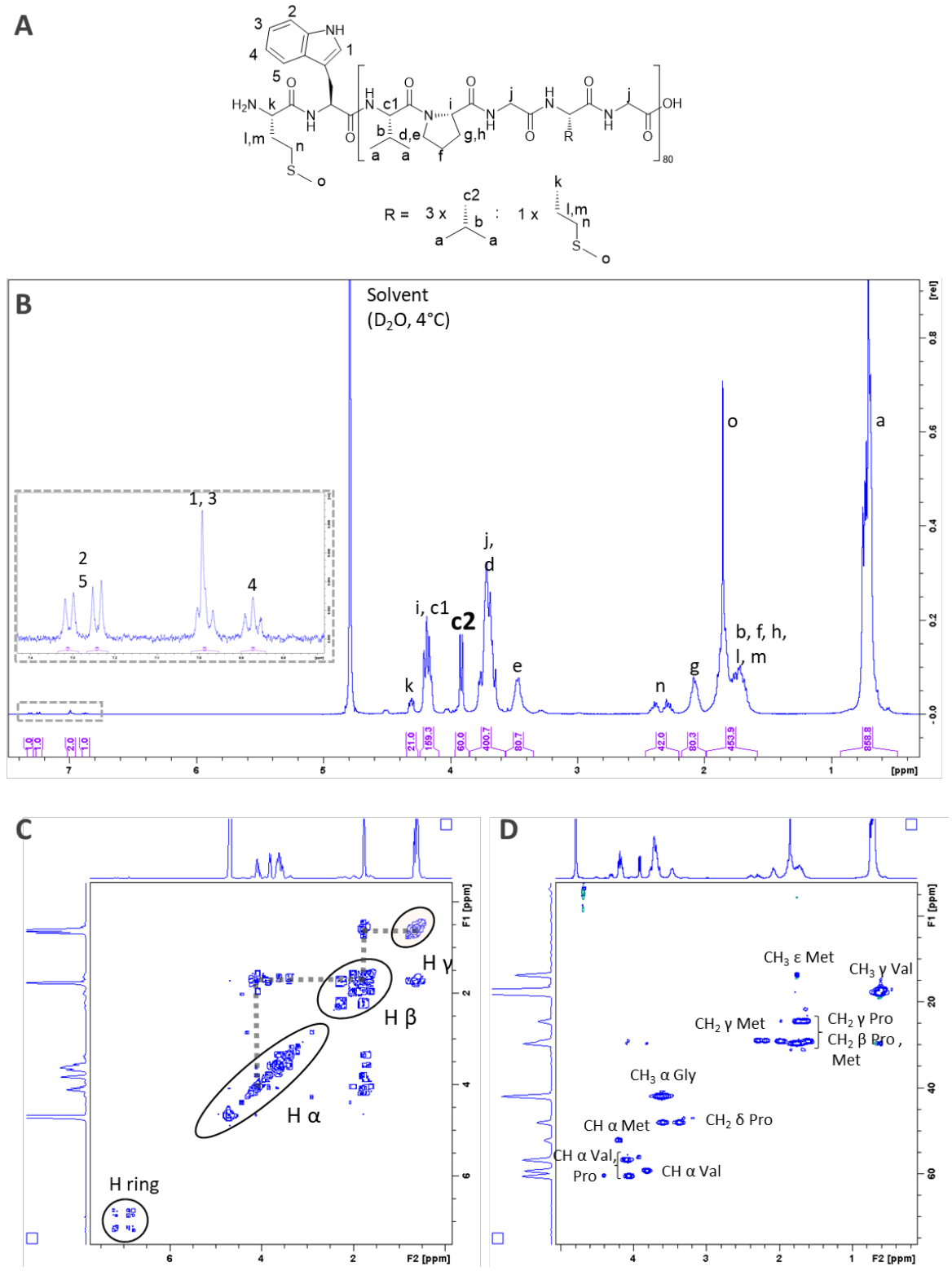

Figure S3: *NMR characterization of ELP[M_1V_3-80] (D_2O, 4°C, 400 MHz). (A) Chemical structure and proton notation. (B) ^{1}H NMR spectrum. Reference for integration: c2 (CH Valine VPGVG, 60 H). (C) COSY spectrum. Coupling between protons in α, β, and γ of the peptide chain and on the aromatic ring. (D) HSQC spectrum. Coupling between adjacent protons and carbons. Similar analyses were performed on ELPn60 and ELPn100. (Data not shown)*

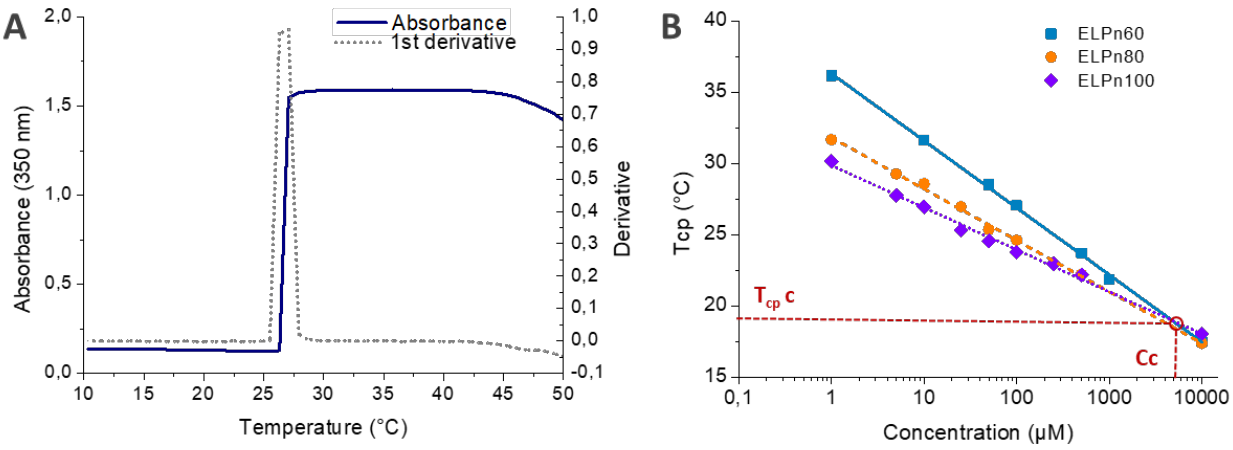

Figure S1: *Characterization of the thermo-responsive properties. (A) Turbidimetry measurement for a solution of ELPn60 at 100 µM in saline TRIS HCl buffer. The T_{cp} is defined as the temperature at the maximum of the 1st derivative. (B) Evolution of T_{cp} with molar concentration for ELPn60, ELPn80, and ELPn100. Fitting with a model "$T_{cp} = a - b * \ln(C)$"[2]. The intersection point between the 3 curves provides the coordinates (C_c and $T_{cp,c}$) of the LCST of the ELP[M_1V_3-n] family.*

ELP[M_1V_3-n]	M_w th (g/mol)	Recombinant production		Molar Mass			Thermoresponsiveness		
		Mean Yield (mg/L)	Number of productions	M_n SEC (g/mol)	M_w SEC (g/mol)	M_w MALDI (g/mol)	T_{cp} at 100 µM (°C)	T_{cp} at 1 µM (°C)	slope b
n = 60	**25,385**	110 (± 25)	10	27,670	28,760	25,417	27	36	2.05
n = 80	**33,700**	117 (± 4)	4	35,830	37,570	33,788	25	32	1.57
n = 100	**42,000**	73 (± 44)	8	44,550	46,130	42,122	24	30	1.29

Figure S2: *Table summarizing the molar mass and the thermo-responsive properties of ELP[M_1V_3-n] (n = 60, 80, 100). Mw th: theoretical molar mass. Slope b: value of the slope in the fitting model "$T_{cp} = a - b * \ln(C)$". $b = k/n$, with k a positive constant and n the number of repetitions of the pentapeptide.*

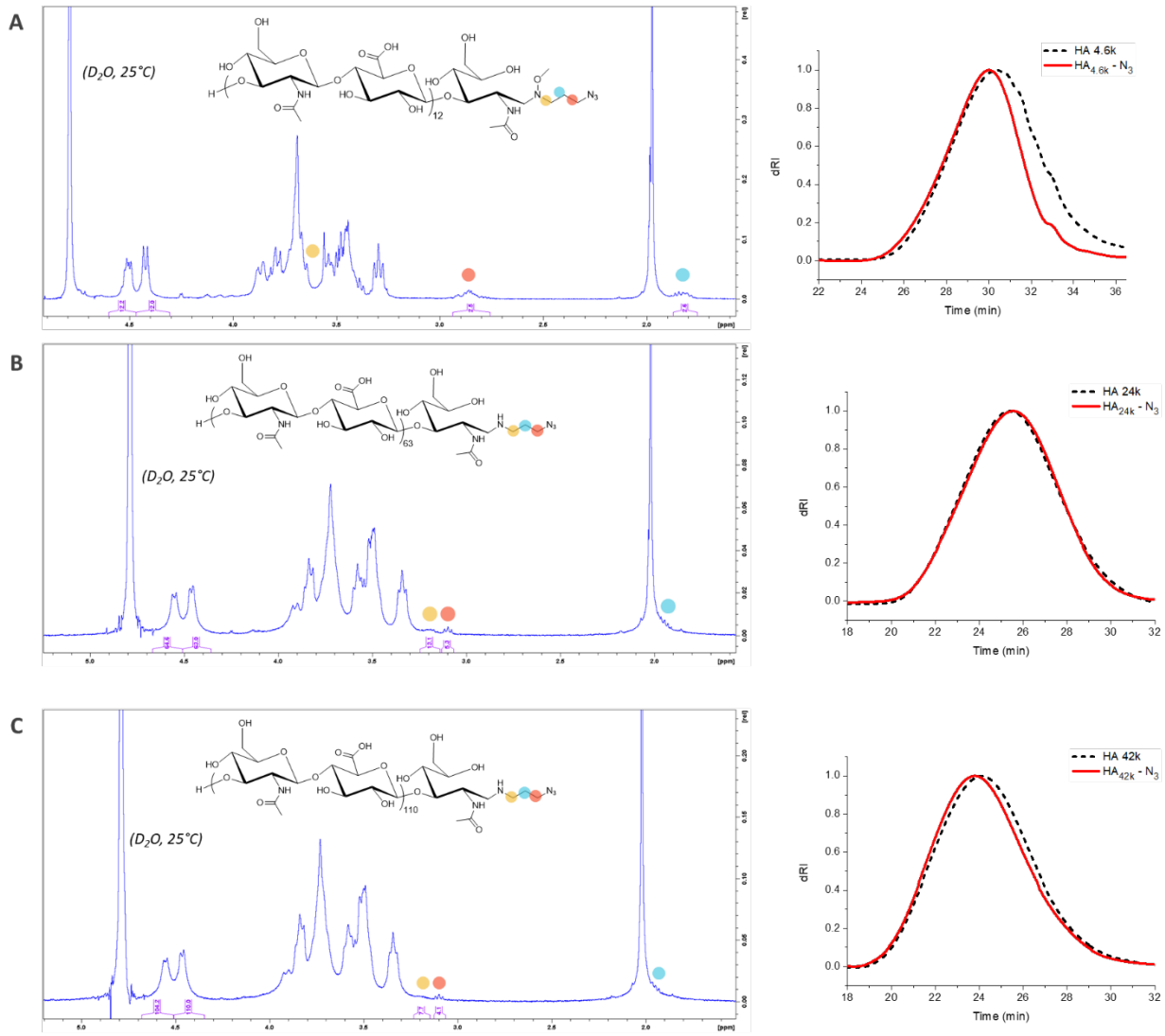

Figure S3: *Characterization of $HA_{4.6k}$-N_3 (A), HA_{24k}-N_3 (B) and HA_{42k}-N_3 (C). Left: ^{1}H NMR spectra (D_2O, 25°C, 400 MHz). Right: SEC chromatograms (phosphate buffer) of HA (black) and HA-N_3 (red).*

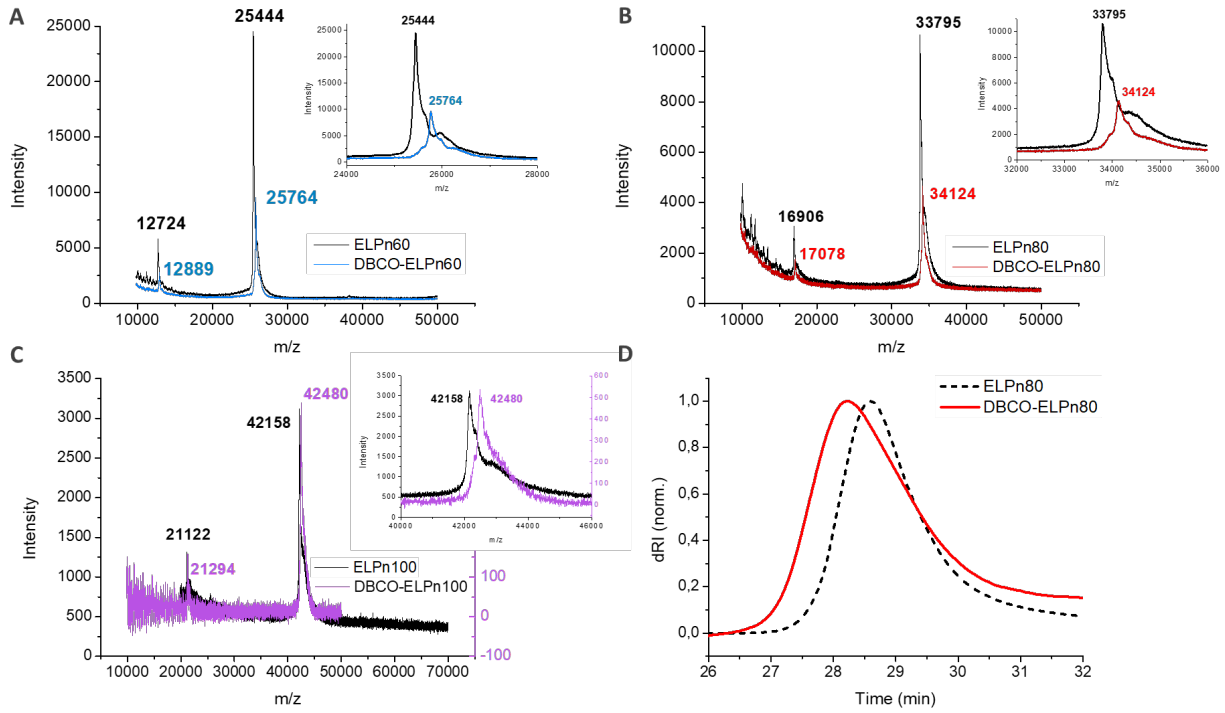

Figure S4: *Characterization of ELP before (black) and after (colored) functionalization with DBCO. A, B, C: MALDI spectrograms for (DBCO-)ELPn, with n = 60, 80,100 respectively. Theoretical m/z shift = +315 g/mol. D: SEC chromatograms of ELPn80 (black) and DBCO-ELPn80 (orange) in phosphate buffer.*

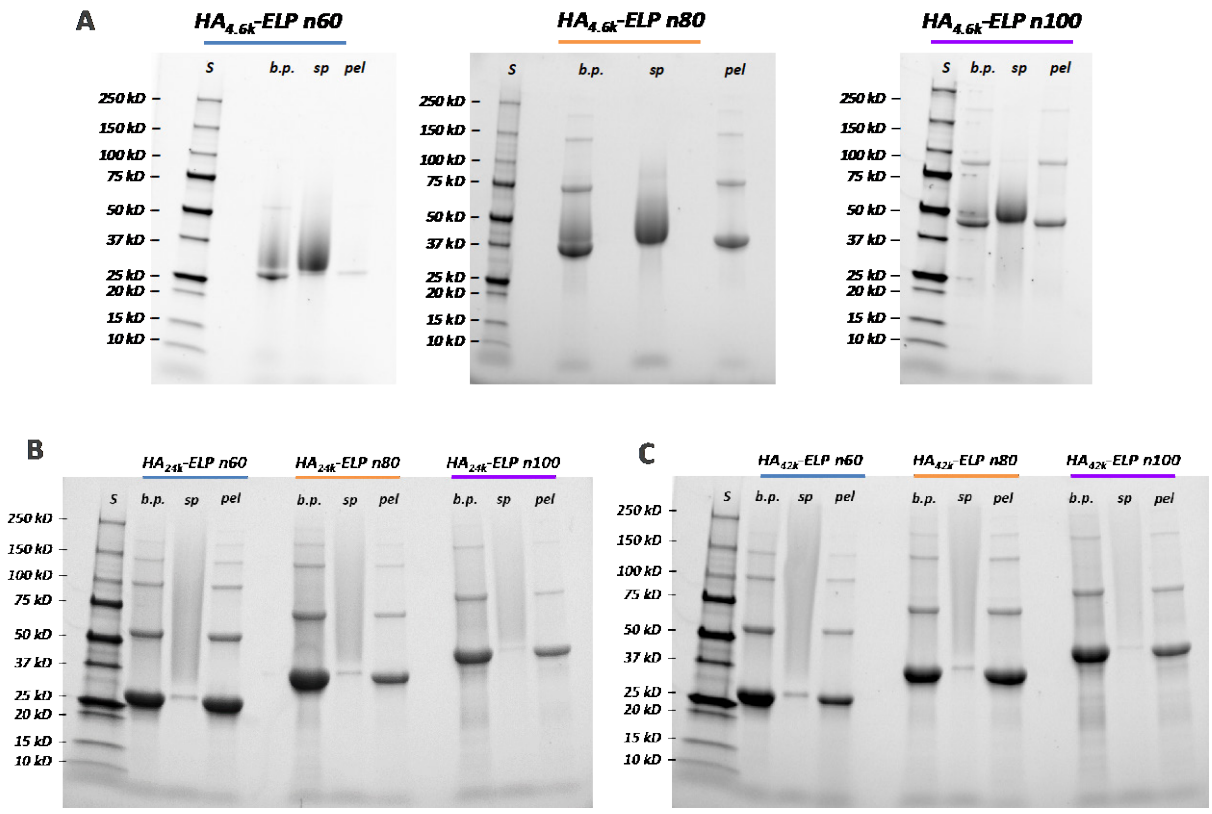

Figure S8: *Characterization of the entire library of bioconjugates by SDS-PAGE. A: $HA_{4.6k}$-ELPn (n=60,80,100); B: HA_{24k}-ELPn (n=60,80,100); C: HA_{42k}-ELPn (n=60,80,100). S: protein size markers; b.p.: reaction medium before purification; sp: supernatant; pel: pellet. B: samples in phosphate buffer. To note, the figure for $HA_{4.6k}$-ELPn80 (panel A, figure in the middle), provided in the main manuscript (Figure 2A), is here shown again for comparison to the other bioconjugates.*

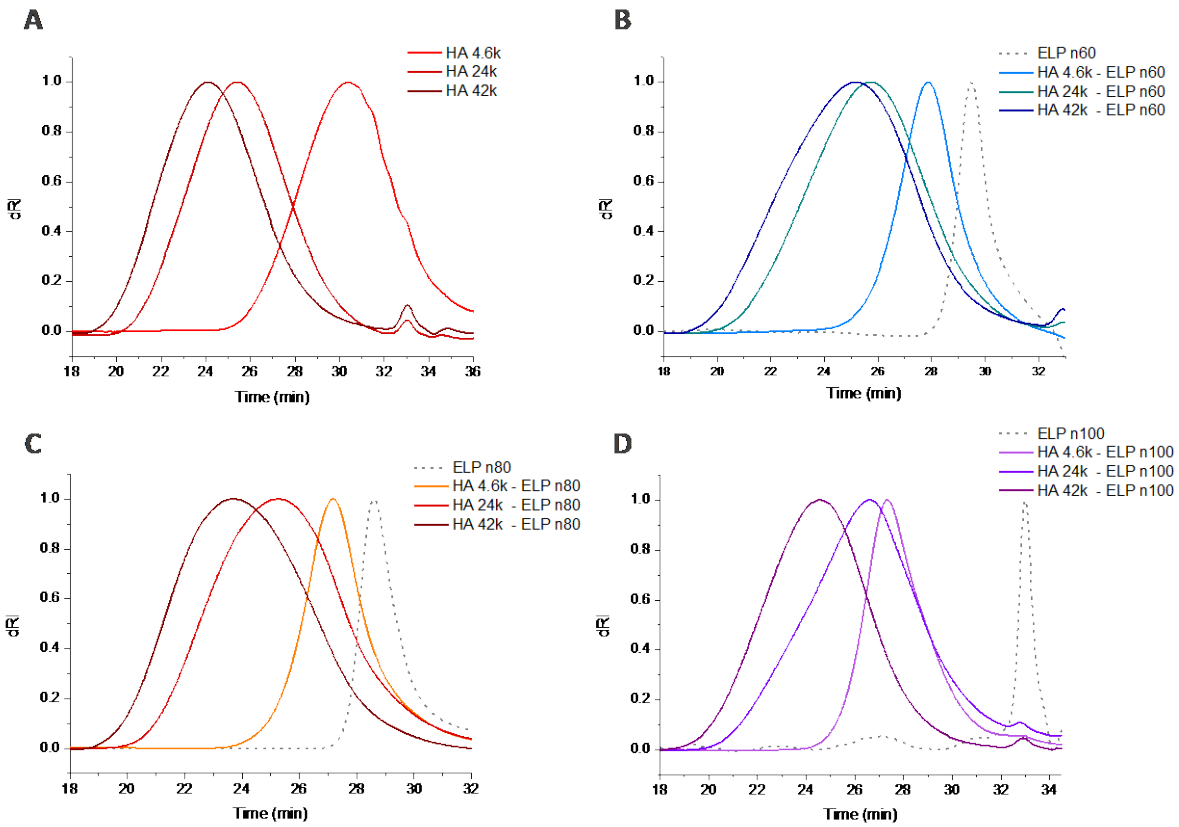

Figure S9: *Characterization of the entire library of bioconjugates by SEC. Normalized SEC chromatograms of A: commercial $HA_{4.6k}$, HA_{24k}, and HA_{42k}; B: HA_{xk}-ELP60; B: HA_{xk}-ELP80; D: HA_{xk}-ELP100. In panels B, C, and D, the chromatogram of the starting ELPn (n=60,80,100) is also included (grey dash). Samples in phosphate buffer.*

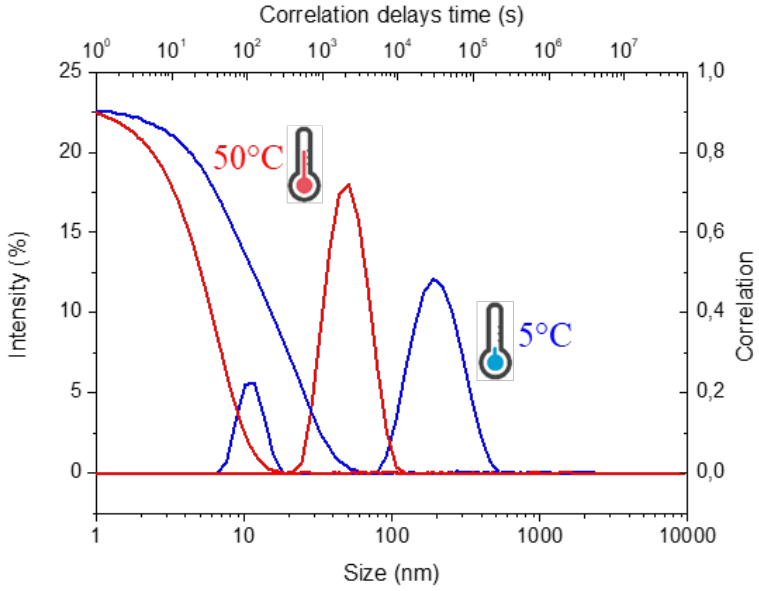

***Figure S10**: Characterization of the self-assembly by DLS for a solution of bioconjugates $HA_{4.6k}$-ELPn80 at 78 µM in PBS. Size distributions and associated correlograms at T<CMT (5°C) and T>CMT (50°C).*

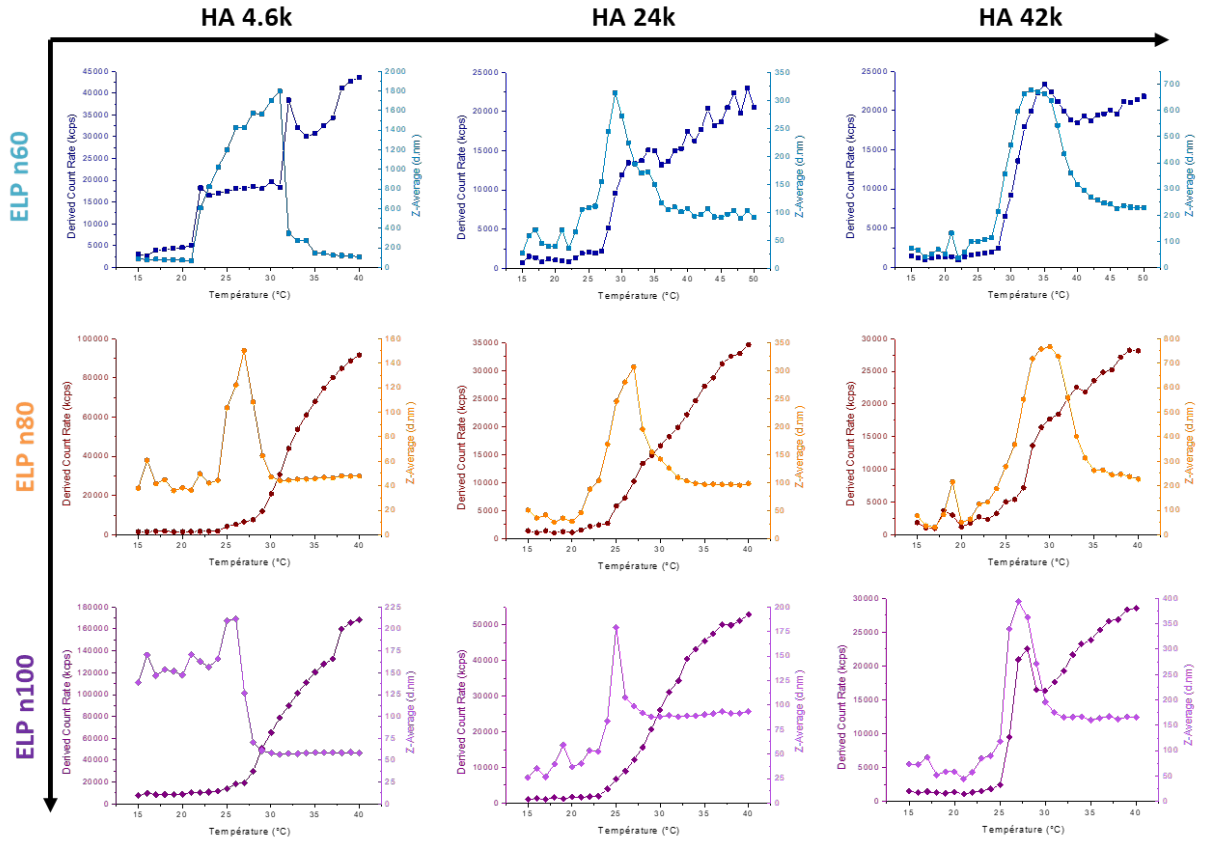

***Figure S11:** Critical Micellar Temperature (CMT) determination by DLS analysis for the whole library of HA-ELP bioconjugates (78 µM in PBS). Evolution of the derived count rate (dark, left axis) and of the z-average (light, right axis) with temperature (heating ramp: 15°C-40°C).*

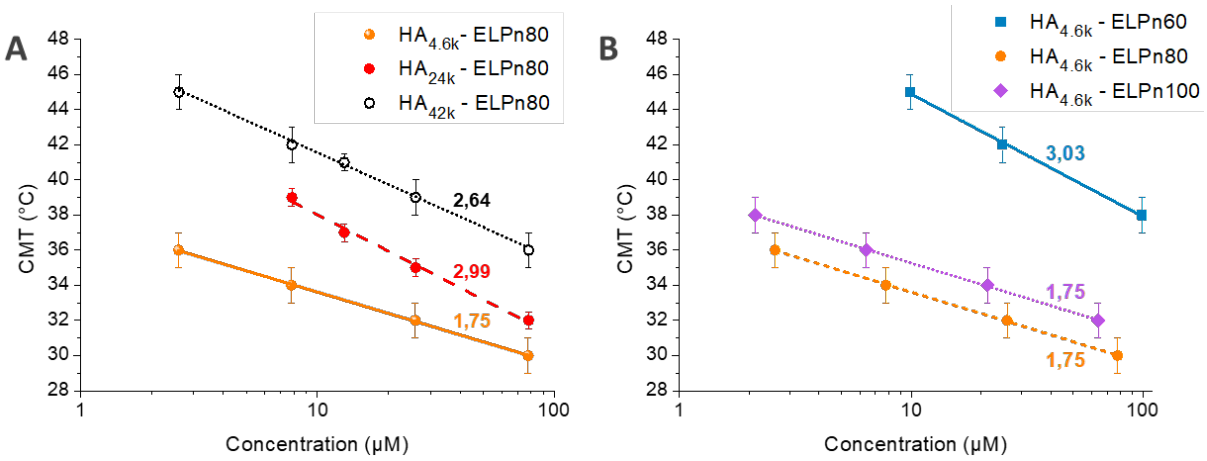

Figure S52: *Evolution of the CMT measured by DLS with the concentration in function of the structure of the bioconjugates. A: varying HA block size. B: varying ELP block size. Fit: CMT = a – b * Ln (C). Values of the slope b displayed on the graphs.*

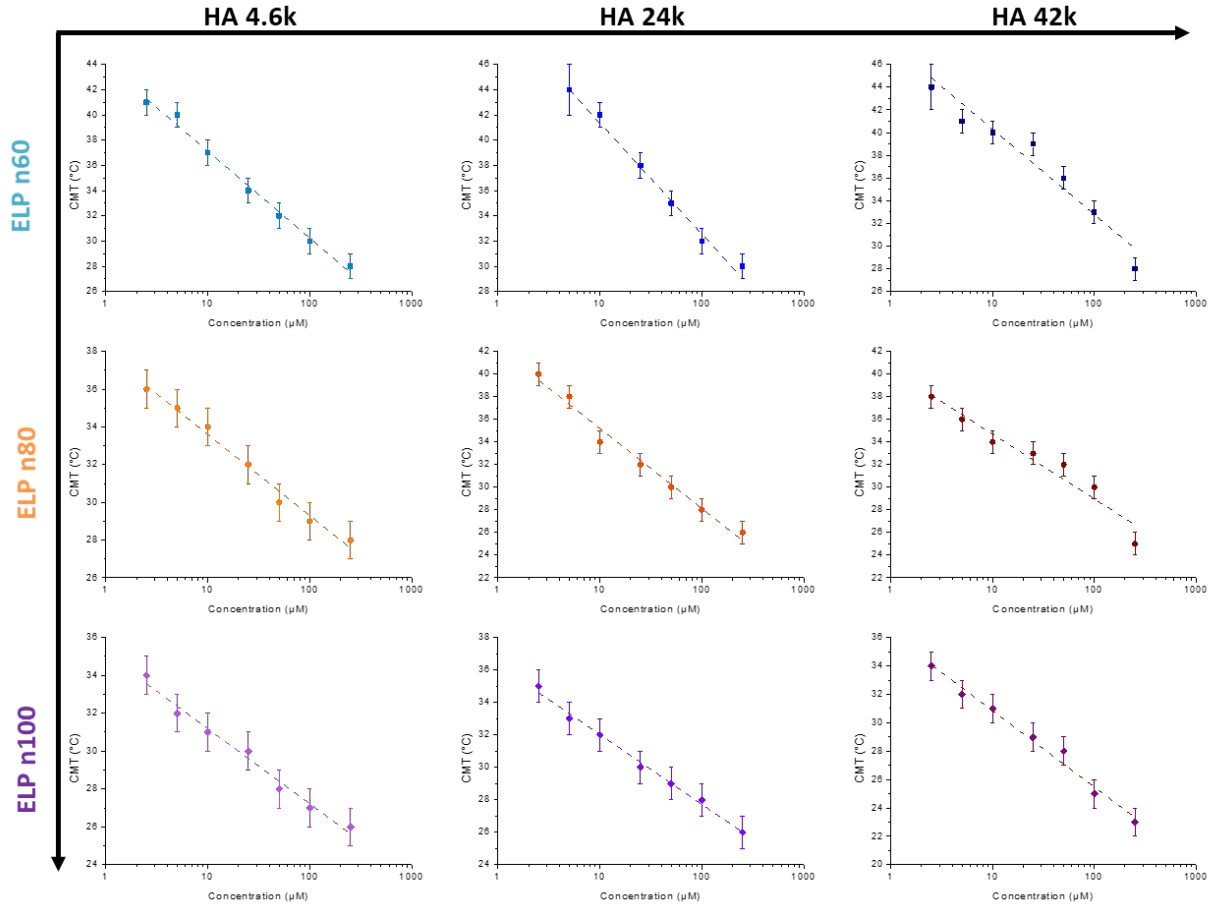

Figure S13: *Evolution of the CMT determined by fluorescence spectroscopy with concentration for the whole library of HA-ELP bioconjugates.*

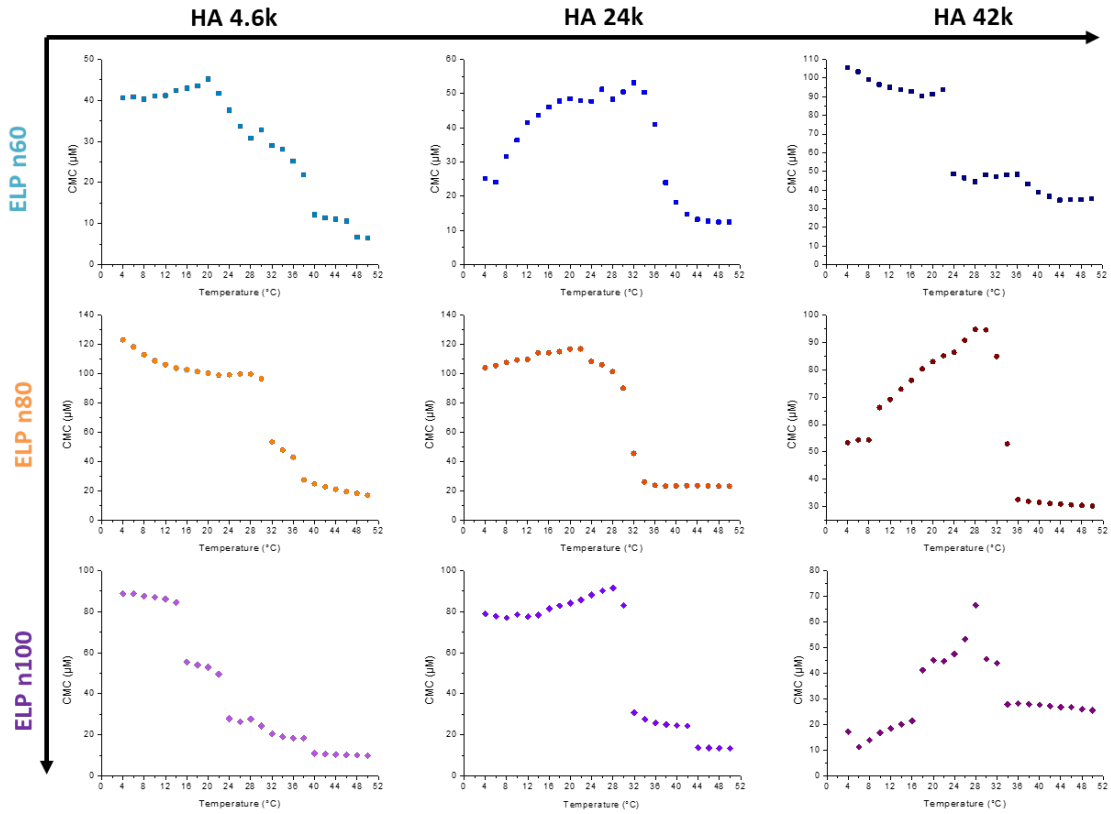

Figure S14: *Evolution of the CMC determined by fluorescence spectroscopy with temperature for the whole library of HA-ELP bioconjugates.*

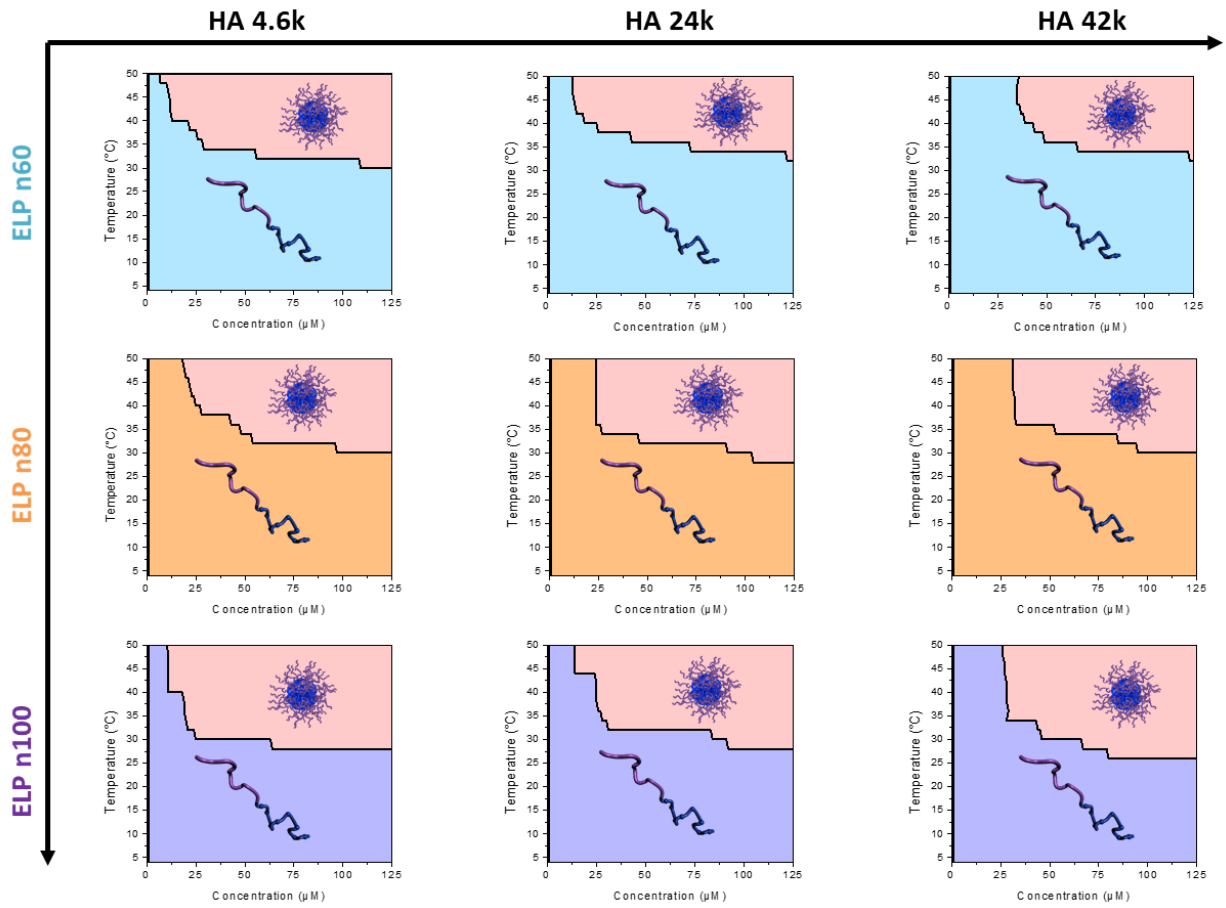

Figure S15: *Phase diagrams of the whole library of HA-ELP bioconjugates. Bottom zone: free chains. Red zone: self-assembled nanoparticles. Coacervate phase not shown.*